2018

Calibration and Uncertainty Analysis of a Fixed-Bed Adsorption Model for CO2 Separation

K. N. Son

J. A. Weibel
Purdue University, jaweibel@purdstinue.edu

J. C. Knox

S V. Garimella
Purdue University, sureshg@purdue.edu

Son, K. N.; Weibel, J. A.; Knox, J. C.; and Garimella, S V., "Calibration and Uncertainty Analysis of a Fixed-Bed Adsorption Model for CO2 Separation" (2018). *CTRC Research Publications.* Paper 337.
http://dx.doi.org/https://doi.org/10.1007/s10450-018-9982-x

Calibration and Uncertainty Analysis of a Fixed-bed Adsorption Model for CO_2 Separation

Karen N. Son[†], Justin A. Weibel[†], James C. Knox[2], and Suresh V. Garimella[, †].*

[†] School of Mechanical Engineering, Purdue University, West Lafayette, Indiana 47907, United States

[‡] George C. Marshall Space Flight Center, National Aeronautics and Space Administration, Huntsville, Alabama 35812, United States

[*]Corresponding author, Tel.: +1 765 494 5621, E-mail address: sureshg@purdue.edu

Abstract

Fixed-bed adsorption is widely used in industrial gas separation and is the primary method for atmosphere revitalization in space. This paper analyzes the uncertainty of a one-dimensional, fixed-bed adsorption model due to uncertainty in several model inputs, namely, the linear-driving-force (LDF) mass transfer coefficient, axial dispersion, heat transfer coefficients, and adsorbent properties. The input parameter uncertainties are determined from a comprehensive survey of experimental data in the literature. The model is first calibrated against experimental data from intra-bed centerline concentration measurements to find the LDF coefficient. We then use this LDF coefficient to extract axial dispersion coefficients from mixed, downstream concentration measurements for both a small-diameter bed (dominated by wall-channeling) and a large-diameter bed (dominated by pellet-driven dispersion). The predicted effluent concentration and temperature profiles are most strongly affected by uncertainty in LDF coefficient, adsorbent density, and void fraction. The uncertainty analysis further reveals that ignoring the effect of wall-channeling on apparent axial dispersion can cause significant error in the predicted breakthrough times of small-diameter beds.

KEYWORDS: uncertainty analysis, fixed-bed adsorption, atmospheric revitalization, linear driving force assumption, axial dispersion

Introduction

Fixed adsorbent beds are used for gas separations across a wide range of applications from industrial chemical processing and thermochemical energy storage to atmospheric revitalization in confined habitations. Simulations are increasingly relied upon in designing such systems to save cost and time over the traditional design-build-test approach. As a direct numerical simulation of such multi-scale systems is computationally intractable, simplified models (*e.g.*, one-dimensional flow) are often employed to predict system performance. Understanding the accuracy of these predictive models is increasingly important as we transition to a simulation-based design and optimization approach.

Uncertainty and sensitivity analyses are formal methods of assessing model accuracy. Sensitivity analyses enable users to rank model inputs by importance; however, a sensitivity analysis alone is insufficient to quantify overall model uncertainty. Such quantification requires a separate analysis to assess the uncertainty in model outputs based on the uncertainty in inputs. While there are numerous studies on the sensitivity of fixed-bed adsorption models to various model inputs, there are few studies that formally asses the uncertainty of such models. We review here studies on the sensitivity of fixed-bed adsorption models to motivate and frame the present uncertainty analysis work.

Sensitivity analyses of one-dimensional, fixed-bed adsorption models have generally focused on the effect of varying process parameters (*e.g.*, flow rate, inlet concentration, bed length) over their operating range on breakthrough curves[1]. Though understanding the effects of process parameters is vital for the operation of a system, studies that only consider these known or easily-measured process parameters do not provide insight into model accuracy caused by uncertainties in other critical input parameters. There are comparatively fewer studies which analyze the uncertainty of

adsorption models due to errors in empirically-predicted inputs such as heat and mass transfer parameters. Most such studies focus on the effect of uncertainties in mass transfer parameters on the breakthrough curve. Refs. 2–17 used models which account for both interparticle and intraparticle transport, and compared the relative sensitivities of multiple mass transfer parameters to determine the dominant mass-transfer mode(s). These studies found that model results are sensitive to mass transfer coefficients and generally, there is a single, dominant mass-transfer mode to which the model is most sensitive. It is well known that intraparticle diffusion can be ignored and the mass-transfer resistance can be approximated by a single parameter termed the linear-driving-force (LDF) coefficient when one mass-transfer mode dominates[18], as is the case for zeolite 5A[19]. Refs. 20–26 evaluated the sensitivity of the breakthrough curve to this LDF coefficient. The LDF approximation is widely used both in the literature and in the industry as a simplified representation of the mass transfer process in fixed-bed adsorption with good results as there is generally one dominant mass-transfer resistance[27,28]. Regardless of the mass-transfer model, it is generally accepted that one-dimensional, fixed-bed adsorption models are sensitive to the mass transfer coefficients if the process is far enough away from the extreme limit of local gas-adsorbent concentration equilibrium.

Other studies focus on the sensitivity of adsorption models to equilibrium isotherm parameters. This includes investigations on the effect of different isotherm types (*e.g.*, linear versus Langmuir, multi-component versus single-component)[1]. It has generally been concluded that nonlinear isotherms are required to model adsorption with a reasonable degree of fidelity[21,23], and that adsorption is highly sensitive to isotherm parameters while desorption is insensitive[23]. A large number of studies investigated only the effect of varying the isotherm parameters for a single isotherm model; Refs. 2,3,5,20,23,26,29 studied the effect on quantitative metrics such as

breakthrough time, while Refs. 4,14,20–22,30–32 evaluated model sensitivity by observation of changes in the slope or position of breakthrough curves. Most of these studies[2–4,21,22,26] evaluated model sensitivities to the Freundlich isotherm parameters. Others investigated sensitivity to the Langmuir isotherm parameters[31], the Langmuir-Freundlich (*i.e.*, Sips) isotherm parameters[5,13], or the Toth isotherm parameters[20,32]. Despite the wide variety of systems and isotherm types considered in these studies, there is a consensus in the literature that one-dimensional, fixed-bed adsorption models are sensitive to both the type of isotherm used (*e.g.*, Freundlich, Langmuir, Toth) and to uncertainties in the empirically determined isotherm parameters[1].

Conclusions in the literature regarding sensitivity to axial dispersion are less consistent; while many researchers concluded that adsorption models are insensitive to axial dispersion[3,4,10,12,14,21,26,30], others found the opposite to be true[16,24,25,33]. Yet others are equivocal in their conclusions. For example, Borina and Pavko[34] note that sensitivity to axial dispersion is a complex function of process parameters such as bed length and flow rate. They found that breakthrough time was insensitive to axial dispersion for a short bed at low velocity (L = 180 cm, $u_\infty = 4.1\times10^{-5}$ m/s) but highly sensitive to axial dispersion for a longer bed at high velocity (L = 1000 cm, $u_\infty = 4.1\times10^{-2}$ m/s). Lu *et al.*[24] found that sensitivity to axial dispersion also depends on the criteria used to define breakthrough time (c/c_0 = 2%, 50%, or 98%), with lower breakthrough concentration criteria (*i.e.*, c/c_0 = 2%) causing the model to be most sensitive to axial dispersion. They concluded that sensitivity to axial dispersion becomes important relative to other parameters as the requirements on effluent concentration become more stringent.

Most of these studies used empirical correlations to predict the axial dispersion coefficient. Axial dispersion is a complex function of flow conditions and bed geometry, with available correlations spanning several orders of magnitude in their predictions[35,36]. While there are many

correlations (both empirical and semi-empirical) that allow researchers to directly predict the axial dispersion of their system without comparing their model directly to experimental data or higher-fidelity simulations, none of these correlations account for every possible mechanism of axial dispersion. Furthermore, the available empirical correlations do not account for wall channeling, causing them to drastically underpredict the apparent axial dispersion in small-diameter beds, such as those used in laboratory experiments to obtain fitted parameters[25,33]. Knox *et al*.[33] investigated the effect of using such empirical correlations to predict axial dispersion when fitting a one-dimensional, fixed-bed adsorption model to typical lab-scale, experimental-breakthrough data. Knox *et al*.[33] focused on the effect of using such predictions of axial dispersion on subsequently fit model parameters (*e.g*., LDF mass transfer coefficient). They found that using empirical prediction of axial dispersion fitted to the effluent caused an error in LDF coefficient and proposed an experimental method for reducing this error using in-bed centerline concentration measurements where the near-wall apparent dispersion effects are minimized.

Some recent studies more deeply investigated the suitability of the axially-disperse plug flow model to describe breakthrough in confined geometries. In small-diameter beds, packing heterogeneities near the wall lead to faster flow around the periphery of the bed. The effects of this bypass flow (also referred to as near-wall channeling) are mitigated by increasing radial dispersion[37] and pellet-to-bed diameter ratio[38]. Two approaches can be used when near-wall channeling effects play a significant role in the hydrodynamics. The first approach uses two-dimensional simulations to account for the radial distribution of velocity (*e.g.*, Augier *et al*.[39]). The second approach maintains the plug-flow assumption and uses a larger, apparent axial dispersion to account for the wall-channeling (*e.g.*, Knox *et al*.[33]).

Compared to the wealth of literature on equilibrium and kinetic parameters for mass transfer, relatively few papers have considered sensitivity to heat transfer parameters[9,21,23,31,40–43]. This is partially due to the simplifying assumption made in many studies[2–8,10–17,24–26,30,32,34] to neglect heat transfer and treat the entire bed as isothermal. This assumption is made despite the fact that system-level models of cyclic pressure and temperature-swing-adsorption processes are known to be highly sensitive to temperature variations[20]. Even studies that account for heat transfer rely on assumptions such as adiabatic walls[21,31,41,43], constant isosteric heat of adsorption[40,42], or local thermal equilibrium (LTE)[21,29,40,41,43]. Sircar *et al.*[40] evaluated the adiabatic wall assumption and concluded that while the breakthrough time is insensitive to the ambient heat loss, the profile of concentration in the bed depends strongly on this quantity. Furthermore, using an adiabatic boundary condition induced considerable error when fitting equilibrium capacity and the kinetic parameters, even when the temperature change in the column is small. In another study, Sircar[42] studied the effect of the fluid-solid heat transfer coefficient on the performance of a pressure swing adsorption system by modeling a single particle and concluded that the LTE assumption is appropriate at high Nusselt numbers ($Nu > 6$). Walton and LeVan[43] showed that assuming a constant isosteric heat of adsorption had minimal impact on plateau temperature, partial pressure, and loading, but a significant impact on breakthrough time compared with temperature-dependent models. The most dramatic difference was observed at the highest adsorbed-phase heat capacity where approximating the isosteric heat as constant led to a severely overestimated breakthrough time.

A comprehensive uncertainty analysis accounting for contributions from all the input parameters of a model that does not make simplifying thermal assumptions is lacking in the literature. We address this deficit in the present study. A high-fidelity model of cylindrical adsorbent beds is

developed which accounts for axial dispersion, local thermal non-equilibrium, nonlinear Toth isotherms, thermodynamically derived heats of adsorption, and temperature-dependent properties. We then follow the calibration method prescribed by Knox *et al*.[33] to independently determine the mass transfer rate (*i.e.*, LDF coefficient) and the axial dispersion coefficient. This work builds upon our prior study[44] which investigated the sensitivity of this same model to inputs, while the present work considers the actual uncertainty in input variables. Upper and lower uncertainty bounds for each of the model inputs are found by comparison of experimental data from the literature to empirical correlations. Model uncertainty is then investigated by independently varying each model input between its individual upper and lower uncertainty bounds and observing the relative change in important output quantities.

Motivation

The Life Support Systems (LSS) project of the National Aeronautics and Space Administration (NASA), a part of the Advanced Exploration Systems program, aims to improve LSS "using the International Space Station's (ISS) state-of-the-art hardware as a point of departure"[45,46]. Deep-space exploration places unprecedented demands on space-launch systems; vehicles will not only be propelled farther than any previous crewed mission, but they also must carry the supplies needed to sustain a crew for years without resupply. This new challenge places added importance on minimizing mass, volume and power loads for all spacecraft systems, including the LSS responsible for the removal of metabolic carbon dioxide (CO_2) from a crewed vehicle.

The LSS project hinges upon the development of predictive simulation tools to reduce the hardware testing requirements in the design of the next generation of atmospheric-revitalization technology[47,48]. Researchers at NASA's Marshall Space Flight Center have developed predictive

models of the ISS Carbon Dioxide Removal Assembly (CDRA) in efforts to create a virtual laboratory through which to optimize the design of the next-generation, air-revitalization system[47]. The CDRA utilizes a fully regenerative thermal/pressure swing adsorption process to remove CO_2 from the ISS cabin air. The CDRA can remove 100% of the metabolic CO_2 generated by six crew members. It operates cyclically, employing two desiccant beds and two adsorbent beds. As one desiccant bed and one adsorbent bed operate in adsorption mode, the other two beds are desorbing (regenerating). Halfway through a cycle, the beds switch modes, providing continuous CO_2 removal capability. The CDRA uses 5A zeolite in the CO_2 adsorbent bed and silica gel in the desiccant bed. Our model follows the same physical assumptions used in the full CDRA, four-bed molecular sieve (4BMS) model[47], including the consideration of a non-constant isosteric heat of adsorption which was a recently added improvement to the 4BMS model. This similarity allows us to extrapolate the results of the present uncertainty analysis to the full 4BMS model.

Experimental Facility

The fixed-bed adsorption breakthrough experiments of Knox *et al*.[33,49] and Son *et al*.[50] are used in this work for model calibration. Cross-sectional drawings of the two test stands from these experiments, respectively called test stand A and B in this paper, have differing bed lengths and adsorbent pellet-to-bed diameter ratios. The two test stands are shown in Figure 1, and their physical properties are listed in Table 1. Test stand A holds a 254 mm (10 in) long bed sandwiched between two layers of glass beads, each 127 mm (5 in) long. This bed is housed in a 47.6 mm (1.87 in) inner diameter canister, which equates to roughly 24 pellets across the inner canister diameter. The bed in test stand B is shorter at 165 mm (6.5 in) in length but is held in a much larger inner canister diameter of 93.6 mm (3.68 in), approximately 42 pellets across. For both test

stands, five exposed-tip thermocouples measure the gas temperatures upstream and downstream of the bed, and at three centerline locations within the bed, as shown in Figure 1.

The thermocouples in test stand A are factory calibrated T-type thermocouples (±1°C accuracy). Test stand A is instrumented with a gas chromatograph (Shimadzu GC-14A with CR601 integrator, ±1.2% of reading uncertainty[49]) which monitors the centerline CO_2 concentration at five axial locations: (1) upstream of the bed, (2) 6.5 mm from the inlet of the bed (*i.e.*, 2.5% of the total bed length), (3) the middle of the bed, (4) 6.5 mm from the exit of the bed, and (5) far downstream of the bed. Total pressure was measured at each of these five-sampling locations in test stand A (Viatran pressure transducer, 0-30 psia range, and ±0.25% full-scale range uncertainty) which was connected to the gas sampling line during a separate pressure-drop test run at the same flow rate used for the breakthrough experiments. The thermocouples in test stand B are calibrated to measure temperature to within ±0.2°C uncertainty using a dry-block calibrator with RTD sensor. Test stand B is instrumented with two continuous-sampling, infrared CO_2 sensors placed upstream and downstream of the bed (Sable Systems CA-10 CO_2 Analyzer, ±1% of reading accuracy over a range of 0-5% CO_2 by volume). In test stand B, the total pressure is measured before and after the bed by two absolute pressure transducers (Honeywell FP2000, 2-172 kPa range and ±0.10% full-scale range uncertainty) in real-time throughout the breakthrough experiment.

Detailed descriptions of the test stands and experimental methods can be found in Refs. 33, 49, and 50. To match conditions in the CDRA, the experiments use zeolite 5A adsorbent at similar superficial velocity (0.28 m/s) and inlet temperature (300 K) during breakthrough. The bed diameters, however, are significantly larger at ~20 pellets across for the bed in test stand A and ~42 pellets across for the bed in test stand B; thus, we expect that the empirically fit axial dispersion coefficients will be much lower than the axial dispersion in a CDRA channel with ~6 pellets across

the bed, where flow channeling, caused by low porosity near the wall, dominates the axial mixing and leads to a high apparent dispersion. Breakthrough test data can be used to calibrate the mass transfer (LDF) coefficient and dispersion coefficient. Prior to the start of breakthrough experiments, test stand A is filled with helium gas and test stand B is filled with N_2; the beds in both stands the are devoid of CO_2. A mixture of N_2 and CO_2 begins flowing into the bed at $t = 0$. The inlet flow is maintained at a superficial velocity of 0.28 m/s and constant CO_2 partial pressure, while the outlet is maintained at a constant total pressure. The CO_2 is adsorbed by the pellets as the gas mixture passes through the bed. Eventually, there is a small, but measurable quantity of CO_2 detected in the bed effluent. The time at which this occurs is termed the initial breakthrough time, t_b. For this work, the breakthrough time is defined as the time at which the effluent concentration first reaches 1% of the influent concentration, c_0. The test continues until the bed is completely saturated, meaning that the effluent concentration matches the influent concentration to within 1%. This occurs at approximately $t = 2$ hr.

Modeling Approach

An axially-dispersed, plug-flow reactor model is developed based on the cylindrical bed geometries shown in Figure 1. We model the breakthrough process as described in the *Experimental Facility* section above. The model is quasi-one-dimensional in that the temperature of the four separate constituents (gas phase, adsorbent, canister wall, and insulation) can differ at the same axial position and are coupled via heat transfer coefficients. Thus, the model requires four separate energy balances, one for each constituent. The model additionally requires two mass balances for the gas phase and adsorbed CO_2 phase. These six governing equations (two mass

balances and four energy balances) are coupled and solved to obtain the CO_2 concentrations and temperatures as a function of time and axial position.

Adsorbed-phase mass balance

The adsorbed phase concentration is computed using the linear-driving-force (LDF) approximation[51]. The physical process of adsorption is controlled by several mass transfer resistances, including macropore, micropore, and surface diffusion. The LDF approximation ignores the concentration gradient within a pellet and lumps these resistances into a single term. It is assumed that the adsorption rate ($\partial q/\partial t$) is linearly proportional to the difference between the adsorbate concentration in the gas phase, q, and the equilibrium adsorbed-phase concentration, q^*,

$$\frac{\partial q}{\partial t} = k_n \left(q^* - q \right), \tag{1}$$

where the constant of proportionality, k_n, is termed the LDF mass transfer coefficient. The equilibrium adsorbed-phase concentration, q^*, corresponds to the CO_2 partial pressure, p_{CO_2}, at the adsorbent temperature, T_s, based on the equilibrium adsorption isotherm as described under *Model inputs* below. The bed is assumed to be initially devoid of CO_2 (*i.e.*, $q(t = 0) = 0$).

Gas-phase mass balance

The gas-phase mass balance is coupled with the adsorbed-phase mass balance via the rate of adsorption. This balance also accounts for advection and axial dispersion through the bed as

$$\frac{\partial c}{\partial t} + \left(\frac{1-\varepsilon}{\varepsilon} \right) \frac{\partial q}{\partial t} - D_{ax} \frac{\partial^2 c}{\partial z^2} = -\frac{\partial (u_1 c)}{\partial z}, \tag{2}$$

where c is the gas-phase concentration of the adsorbate (*i.e.*, CO_2). The axial dispersion coefficient, D_{ax}, is calculated from the parametric equation of Edwards and Richardson[52] as described in the upcoming *Model inputs* section. We represent the experimental boundary

conditions in our model with a constant flux boundary condition at the inlet and the Danckwert's boundary condition at the outlet, respectively defined as

$$-D_{\text{ax}} \left.\frac{\partial c}{\partial z}\right|_{z=0} = \frac{u_\infty}{\varepsilon}\left(c_0 - c\right) \quad \text{and} \quad \left.\frac{\partial c}{\partial z}\right|_{z=L} = 0 \ . \tag{3}$$

Energy balance

Separate energy balance equations for the gas, adsorbent, canister wall, and insulation are included in the model to account for local thermal non-equilibrium. An analysis of the time constants for energy flow between these four constituents indicates that none can be neglected. It is critical to account for diabatic effects due to the large thermal mass of the container. All four energy balances account for transient heat storage and heat transfer between the separate regions. In addition to these terms, the adsorbent energy balance includes a heat of adsorption term that accounts for the exothermic and endothermic nature of adsorption and desorption, respectively.

The gas-phase energy balance includes transient heat storage, axial dispersion, advection, and convective heat transfer to the adsorbent and canister wall,

$$\varepsilon A_{\text{fr}} \rho_{\text{g}} c_{p,\text{g}} \frac{\partial T_{\text{g}}}{\partial t} = \varepsilon A_{\text{fr}} k_{\text{eff}} \frac{\partial^2 T_{\text{g}}}{\partial z^2} - \varepsilon A_{\text{fr}} \rho_{\text{g}} c_{p,\text{g}} u_{\text{i}} \frac{\partial T_{\text{g}}}{\partial z} + A_{\text{fr}} \left(\frac{A_{\text{s}}}{V_{\text{bed}}}\right) h_{\text{g-s}} \left(T_{\text{s}} - T_{\text{g}}\right) + \pi d_{\text{can,in}} h_{\text{g-can}} \left(T_{\text{can}} - T_{\text{g}}\right) , \tag{4}$$

where $h_{\text{g-s}}$ is the convection coefficient between the gas and adsorbent, $h_{\text{g-can}}$ is the convection coefficient between the gas and canister wall. The effective axial thermal conductivity, k_{eff}, accounts for both the adsorbent- and gas-phase conductivities as well as axial thermal dispersion due to mixing. These coefficients are calculated using empirical correlations as described in the *Model inputs* section below.

The adsorbent-phase energy balance accounts for transient storage, convective heat loss to the gas, and the heat of adsorption, but neglects axial conduction as the gas-phase energy balance already accounts for the adsorbent-bed conductivity,

$$A_{\mathrm{fr}}\left(1-\varepsilon\right)\rho_{\mathrm{env}}c_{p,\mathrm{s}}\frac{\partial T_{\mathrm{s}}}{\partial t}=A_{\mathrm{fr}}\frac{A_{\mathrm{s}}}{V_{\mathrm{bed}}}h_{\mathrm{g\text{-}s}}\left(T_{\mathrm{g}}-T_{\mathrm{s}}\right)-\left(1-\varepsilon\right)A_{\mathrm{fr}}\lambda\frac{\partial q}{\partial t}, \qquad 5$$

where A_{s} is the pellet external surface area. The isosteric heat of adsorption, λ, is derived from the Clausius-Clapeyron relationship as will be described further in the *Model inputs* section.

The canister wall energy balance includes transient energy storage, axial conduction, and heat transfer with the internal gas-phase and the external insulation,

$$A_{\mathrm{can}}\rho_{\mathrm{can}}c_{p,\mathrm{can}}\frac{\partial T_{\mathrm{can}}}{\partial t}-A_{\mathrm{can}}k_{\mathrm{can}}\frac{\partial^2 T_{\mathrm{can}}}{\partial z^2}=\pi d_{\mathrm{can,in}}h_{\mathrm{g\text{-}can}}\left(T_{\mathrm{g}}-T_{\mathrm{can}}\right)+\pi d_{\mathrm{can,out}}h_{\mathrm{can\text{-}ins}}\left(T_{\mathrm{ins}}-T_{\mathrm{can}}\right), \qquad 6$$

where A_{can} is the cross-sectional area of the canister wall and $h_{\mathrm{can–ins}}$ is the heat transfer coefficient between the canister and the insulation. A heat transfer coefficient of $h_{\mathrm{can–ins}}$ = 3 W/(m^2 K) is assumed for both test stands having insulation loosely affixed to the canister wall.

The insulation energy balance accounts for transient energy storage, axial conduction, and heat transfer with the canister and ambient air,

$$A_{\mathrm{ins}}\rho_{\mathrm{ins}}c_{p,\mathrm{ins}}\frac{\partial T_{\mathrm{ins}}}{\partial t}-A_{\mathrm{ins}}k_{\mathrm{ins}}\frac{\partial^2 T_{\mathrm{ins}}}{\partial z^2}=\pi d_{\mathrm{ins,in}}h_{\mathrm{can\text{-}ins}}\left(T_{\mathrm{can}}-T_{\mathrm{ins}}\right)+\pi d_{\mathrm{ins,out}}h_{\mathrm{ins\text{-}amb}}\left(T_{\mathrm{amb}}-T_{\mathrm{ins}}\right), \qquad 7$$

where A_{ins} is the cross-sectional area of the insulation, and the heat transfer coefficient between the insulation and the ambient is assumed to have a value of $h_{\mathrm{ins–amb}}$ = 3 W/(m^2 K).

Model inputs

The model described in the *Mass balance* and *Energy balance* sections above calls for several input parameters to predict the temperatures and concentrations within the bed. Table 1 provides

the geometric dimensions and material properties of the adsorbent, canister, and insulation of the two test stands. The properties of the CO_2 and N_2 gas mixture are computed assuming that they are ideal gases and accounting for local temperature, pressure, and composition[53]. Table 2 summarizes the inlet and initial conditions measured during the breakthrough experiments[33,50]. These conditions, representative of the conditions in the CDRA during adsorption, are used for all simulations in this paper. The remaining model input parameters are either predicted from empirical correlations or directly fit to experimental data. These inputs can generally be categorized as heat transfer coefficients, bed transport properties, or equilibrium isotherm parameters.

The empirical correlations used to predict the heat transfer coefficients and bed transport properties are expressed in terms of the dimensionless Prandtl, Schmidt, and Peclet numbers defined in the *Notation* section. A dimensionless pellet Reynolds number is also used in these correlations, defined using the superficial fluid velocity and the pellet diameter as the length scale,

$$Re_{\mathrm{p}} = \frac{u_{\infty} d_{\mathrm{p}} \rho_{\mathrm{g}}}{\mu_{\mathrm{g}}} \ . \tag{8}$$

The interfacial gas-adsorbent heat transfer coefficient, $h_{\mathrm{g\text{-}s}}$, is predicted from the empirical correlation of Wakao *et al.*[54],

$$Nu_{\mathrm{g\text{-}s}} = \frac{h_{\mathrm{g\text{-}s}} d_{\mathrm{p}}}{k_{\mathrm{g}}} = 2 + 1.1 Pr_{\mathrm{g}}^{1/3} Re_{\mathrm{p}}^{0.6} \ . \tag{9}$$

The heat transfer coefficient between the gas and inner canister wall, $h_{\mathrm{g\text{-}can}}$, is predicted using the empirical correlation from Li and Finlayson[55] as

$$Nu_{\mathrm{g\text{-}can}} = \frac{h_{\mathrm{g\text{-}can}} d_{\mathrm{can,in}}}{k_{\mathrm{g}}} = 2.03 Re_{\mathrm{p}}^{0.8} e^{\left(-6 d_{\mathrm{p}} / d_{\mathrm{can,in}}\right)} \ . \tag{10}$$

The effective axial thermal conductivity is calculated from the correlation of Yagi *et al.*[56] as

$$k_{\text{eff}} = k_{\text{g}}\left(\frac{k_{\text{eff}}^{0}}{k_{\text{g}}} + 0.75 Pr Re_{\text{p}}\right), \tag{11}$$

where the effective axial thermal conductivity of a quiescent bed of spherical particles is given by the Krupiczka[57] equation,

$$k_{\text{eff}}^{0} = k_{\text{g}}\left(\frac{k_{\text{s}}}{k_{\text{g}}}\right)^{n} \quad \text{where} \quad n = 0.280 - 0.757\log_{10}\left(\frac{k_{\text{s}}}{k_{\text{g}}}\right). \tag{12}$$

The axial dispersion is predicted following the method described by Langer *et al*.[58] This method expresses the axial dispersion coefficient for the j^{th} species, $D_{\text{ax},j}$, in dimensionless form as

$$\frac{1}{Pe_{j}} = \frac{D_{\text{ax},j}}{d_{\text{p}}u_{\text{i}}} = \frac{\tau\varepsilon}{Re_{\text{p}}Sc_{j}} + \frac{Pe_{\infty}^{-1}}{1 + \dfrac{\beta\tau\varepsilon}{Re_{\text{p}}Sc_{j}}}, \tag{13}$$

where τ and β are empirically fit constants respectively termed the tortuosity and radial dispersion factor, Pe_{∞} is the Peclet number at infinite velocity, and Sc_j is the Schmidt number for the j^{th} species,

$$Sc_{j} = \frac{\mu_{\text{g}}}{\rho_{\text{g}}D_{\text{M},j}}. \tag{14}$$

We find the molecular diffusivity of component j in the mixture using the relation given by Fairbanks and Wilke[59],

$$D_{\text{M},j} = \frac{1 - y_{j}}{\sum_{k \neq j} y_{k}/D_{jk}}, \tag{15}$$

where D_{jk} is the binary diffusion coefficient of species j in species k calculated from the kinetic theory of gases[60]. The coefficients τ and β in eq 13 were empirically determined by Edwards and Richardson[52] for flow through a uniformly packed bed of non-porous spherical particles to be 0.73 and 13, respectively. This correlation approximates only the pellet-driven dispersion and is valid

for flow where $0.008 < Re_p < 50$ and $0.377 \text{ mm} < d_p < 6 \text{ mm}$. Theoretically, at infinite velocity, $Pe_\infty = 2$; however, experimental observations show that Pe_∞ a strong function of pellet diameter[58]:

$$Pe_\infty = \begin{cases} 6.7 \times \left(d_p / [cm] \right) & d_p \le 0.3 \text{ cm} \\ 2.0 & 0.3 \text{ cm} < d_p \end{cases} . \quad 16$$

We use this empirically observed expression for Pe_∞ when calculating D_{ax} in eq 13.

The equilibrium adsorbed-phase concentration is calculated using the Toth equilibrium adsorption isotherm[61] as

$$q^* = \frac{ap}{\left[1 + (bp)^t\right]^{1/t}}; \quad b = b_0 \exp\left(E/T\right) \\ a = a_0 \exp\left(E/T\right) \qquad t = t_0 + c/T , \quad 17$$

where a is the saturation capacity, b is an equilibrium constant, E is the activation energy or energy of adsorption, and t is the heterogeneity parameter. Parameters a, b, and t are temperature-dependent as shown, whereas a_0, b_0, and t_0 are system-dependent, adsorption-isotherm parameters[62] given in Table 3. The isosteric heat of adsorption, λ, is derived from the Clausius-Clapeyron relationship for the Toth isotherm as

$$\lambda = \frac{a \rho_{env} p_{CO_2}}{\left(1 + \left(b \cdot p_{CO_2}\right)^t\right)^{1/t}} , \quad 18$$

where p_{CO_2} is the partial pressure of CO_2 and a, b, and t are the temperature-dependent parameters from the Toth isotherm shown in eq 17.

Uncertainty Bounds of Model Input Parameters

We compare the available empirical correlations with published experimental data to estimate the uncertainty in the heat transfer coefficients, axial dispersion, and effective axial thermal

conductivity. Experimental data were first collected from the literature for each parameter. The empirical equations were then compared to these experimental data and modified to form upper and lower uncertainty bounds that encompass 95% of all experimental measurements. Experimental data for the gas-adsorbent Nusselt number, $Nu_{g\text{-}s}$, as a function of $Pr^{1/3}Re_p^{0.6}$ taken from Wakao and Kagei[63] (and originally published in Refs. 64–74) are reproduced in Figure 2 along with the empirical correlation by Wakao *et al*.[54] (solid line). The coefficient of the $Pr^{1/3}Re_p^{0.6}$ term in the Wakao *et al.*[54] correlation was varied to obtain upper and lower uncertainty bounds (dashed lines) encompassing 95% of all the experimental data. Similarly, for the gas-wall Nusselt number, the coefficient of the $Re_p^{0.79}$ term in the Li and Finlayson[55] correlation was varied to obtain upper and lower uncertainty bounds (dashed lines) encompassing 95% of all the experimental data as shown in Figure 3. The experimental data in Figure 3 were taken from Li and Finlayson's[55] review of the literature and were originally published in Refs. 75 and 76.

A similar approach was taken to find upper and lower uncertainty bounds for the axial dispersion term. Delgado[35,36] compiled experimental measurements of axial dispersion from several authors[52,77–83]. These data were compared with the Langer *et al*.[58] correlation shown in eq 13. The empirical fits of Scott *et al.*[84] ($\tau = 0.57$, $\beta = 42$) and Wicke[85] ($\tau = 1$, $\beta = 0$) provide the widest range of predicted values for D_{ax}, encompassing 92% of the experimental data shown in Figure 4. We take these two correlations to be the upper and lower bounds on the axial dispersion coefficient.

Özgümüş *et al*.[86] reviewed experimental studies measuring effective axial thermal conductivity for granular packed beds with a variety of bed materials and Reynolds numbers ranging from 0.001 to 3000. We compiled data from those studies[56,87–91] which used spherical particles in a flowing gas (as opposed to water or other liquids). These data included a wide range of particle materials ranging from low thermal conductivity glass, k_s = 0.1 W/(m K), to high thermal conductivity

nickel, k_s = 90 W/(m K). To account for the different particle and fluid properties, the quiescent-bed effective axial thermal conductivity, k_{eff}^{0}, was calculated for each experiment using the Krupiczka[57] equation (Eq 12). We then subtract k_{eff}^{0} from the reported k_{eff} and divided by the gas thermal conductivity, k_g, to obtain the normalized effective axial thermal conductivity, $k_{\text{eff}}/k_g - k_{\text{eff}}^{0}/k_g$. The normalized effective axial thermal conductivity is plotted against the product of Prandtl and Reynolds numbers, $PrRe_p$, along with the empirical correlation by Yagi *et al.*[56] (solid line) in Figure 5. The coefficient of the $PrRe_p$ term in the Yagi *et al.*[56] correlation was then varied to obtain upper and lower uncertainty bounds (dashed lines) encompassing 95% of all the experimental data.

The uncertainty in void fraction and pellet density comes directly from the uncertainty of measured values for test stand B as described by Son *et al.*[50]. The insulation-ambient heat transfer coefficient uncertainty comes from the typical full range of free-convection heat transfer coefficients given by Incropera *et al.*[92]. In the absence of a similar range of possible values for the canister-insulation heat transfer coefficient, we consider the two most extreme cases, an adiabatic interface ($h_{\text{can-ins}} \rightarrow 0$) and an isothermal interface ($h_{\text{can-ins}} \rightarrow \infty$). Knox *et al.*[33,49] found that the uncertainty in LDF due to uncertainty in *ad hoc* prediction of axial dispersion when fitting to experimental data (following the method used in the present work) is approximately ±5%.

It is noted that we do not consider uncertainty in isotherm parameters, for which the adsorption model sensitivities have been extensively characterized and are well-known[2–5,13,20–23,26,30–32]. Thermophysical properties for the canister wall, insulation, and gas mixtures are well known and not considered in this uncertainty analysis. The model uncertainty due to other inputs, such as the geometric dimensions of the bed and inlet conditions, is also not studied because these quantities can be trivially and accurately measured.

Solution Procedure

The governing equations as given by eqs 1–7 are coupled and solved in COMSOL Multiphysics[93]. A one-dimensional mesh is generated with a uniform element size of 1% of the total bed length. The PARDISO algorithm—a direct method based on LU decomposition—is used to solve linear equations and the Newton automatic highly nonlinear method to solve nonlinear equations. The solver uses the backward differentiation formula to dynamically modify the time step and improve computation time; we impose an initial time step of 1×10^{-8} s and a maximum time step of 120 s to improve stability. Convergence is reached when the relative residuals drop below 10^{-4} for all dependent variables, namely CO_2 concentration in the gas phase and adsorbed phase, pressure, and temperatures of the adsorbent, gas, canister, and insulation.

Results

The model is first calibrated using experimental data to determine the LDF coefficient, k_n, and the axial dispersion coefficient, D_{ax}. Then, an uncertainty analysis is performed by varying each model input between its upper and lower uncertainty bounds, as defined in the *Model inputs* section above, and observing the relative change in important output quantities.

Model calibration

Determining the axial dispersion coefficient from experiments using mixed, downstream concentration measurements is inaccurate for a small-diameter bed where wall channeling effects dominate the axial mixing behavior. Available empirical correlations for axial dispersion do not capture the influence of channeling in the near-wall region, as they are designed to predict pellet-driven axial dispersion[35]. Knox *et al.*[33] described a method to more accurately obtain the LDF coefficient from small-diameter reactors by using centerline measurements of concentration

immediately before the exit of the bed. We follow this procedure in the current work to independently extract the LDF and axial dispersion coefficients from the experimental measurements of test stand A. The procedure assumes that dispersion in the center of the bed (far from the canister wall) is pellet-driven, and thus the axial dispersion at the centerline of a bed can be accurately predicted by empirical correlations. Using this prediction of axial dispersion from correlations as an input, the model can then be fit to the centerline measurement of concentration by varying the value of the LDF coefficient; the value that provides the best fit is taken as the LDF coefficient extracted from this calibration process.

To extract the LDF coefficient from test stand A, we simulate breakthrough for LDF coefficients varying from 1.75×10^{-3} s^{-1} to 2.4×10^{-3} s^{-1} at increments of 5×10^{-5} s^{-1}, while using the Edward and Richardson correlation[52] to predict axial dispersion at the inlet conditions ($D_{ax} = 1.13\times10^{-3}$ m^2/s). The temporal, gas-phase-CO_2 concentration is then compared with experimental data at 97.5% of the bed length (z = 247.5 mm). Figure 6a shows the time dependence of the concentration of CO_2 at the bed exit breakthrough from the best-fit simulation (black line) alongside experimental measurements of the centerline concentration (red diamonds) for test stand A. This plot is commonly referred to as the breakthrough curve. The gray region in Figure 6a marks the span of the simulated breakthrough curves for LDF coefficient. Initially (at t = 0) the adsorbent is devoid of CO_2, and when the N_2-CO_2 gas mixture first enters the bed, it adheres to the first few layers of adsorbent, filling up the most easily accessed surface area with monolayers of CO_2. As time progresses, the adsorbent near the bed entrance becomes saturated, and the CO_2 penetrates farther into the bed; however, the CO_2 does not reach the bed exit until most of the bed becomes saturated. The breakthrough point as defined herein occurs when the CO_2 concentration in the effluent reaches 1% of the influent concentration (c/c_0 = 1%); this occurs at t = 0.45 hr in Figure 6a. Due

to the finite rate of adsorption, a diffuse concentration front forms as the CO_2 progresses through the bed. This diffuse front is evident from the S-shaped portion of the breakthrough curve which shows a sharp initial rise in concentration near the breakthrough time and a gradual tapering off as the effluent approaches the influent concentration. The difference in curvature at these two locations is explained by the concentration dependence of the rate of adsorption. The rate of adsorption is linearly proportional to the difference between the current and equilibrium concentrations of the adsorbed phase. Thus, the curvature of the effluent concentration is more gradual at the end of the test, when the bed is nearly saturated, compared with the sharp curvature seen in the initial concentration rise at breakthrough. To evaluate the sum of squared errors (SSE) between the model prediction and the sparse experimental data, a cubic spline is used to interpolate values of experimental concentration (see red line in Figure 6a). Note that the saturation term of the Toth isotherm was increased by 16% to shift the model predictions along the time axis to be in closest agreement with the experimental data at the midpoint of the breakthrough curve. This is necessary because the isotherm parameters used in the model were not developed for the specific zeolite 5A formulation used in this study; furthermore, this capacity change has no influence on the slope of the curve and is thus inconsequential to the resulting best-fit k_n value. Only data in the middle 50% of the concentration range are used to compute the SSE as indicated by the dashed blue horizontal lines in Figure 6a. This is done to fit the LDF to the linear portion of the breakthrough curve. Figure 6b shows the SSE as a function of the LDF coefficient. The minimum SSE corresponds to an LDF coefficient of $k_n = 2.1 \times 10^{-3}$ s^{-1}.

Using this LDF value, the effective axial dispersion of the entire bed (accounting for both the effects of pellet-driven dispersion and wall channeling) is determined by fitting the model predictions to the concentration of the mixed effluent, measured far downstream of the bed.

Breakthrough is simulated for axial dispersion coefficients varying from 1×10^{-4} m^2/s to 1 m^2/s in logarithmic steps (forty steps per decade). Figure 7a shows the breakthrough curve from the best-fit simulation (black line) alongside experimental measurements of the mixed downstream concentration (red diamonds) in test stand A, and Figure 7b shows the SSE as a function of axial dispersion coefficient. Again, for comparing the simulated concentration with experimental data, a cubic spline is used to interpolate values at the simulated time steps, and only data in the middle 50% of the concentration range (indicated by the dashed blue horizontal lines in Figure 7a) are used to compute the SSE. The minimum SSE corresponds to an axial dispersion coefficient of D_{ax} = 1.2×10^{-2} m^2/s which is one order of magnitude larger than the axial dispersion coefficient predicted from the Edwards and Richardson[47] correlation, $D_{ax} = 1.13\times10^{-3}$ m^2/s. We attribute this significant difference to wall channeling effects that dwarf axial dispersion in beds with small pellet-to-bed diameter ratios. Our findings are consistent with those of Knox *et al*.[33], who also calibrated a one-dimensional adsorption model to experimental data from the same test stand. We attribute slight differences from their calibrated LDF and axial dispersion coefficients, 2.3×10^{-3} s^{-1} and 1.3×10^{-2} m^2/s respectively, to differences between our modeling approaches. Namely, the present model uses the Clausius-Clapeyron equation to determine the temperature-dependent isosteric heat of adsorption and separately models the canister wall and insulation, whereas Ref. 33 uses a constant heat of adsorption and combines the insulation and canister-wall energy equations. Additionally, we account for the effect of pellet diameter on Pe_∞[58], a term in the Edwards and Richardson[52] correlation, while Ref. 33 assumes that $Pe_\infty = 2$.

Unlike test stand A, test stand B is not instrumented to measure the centerline CO_2 concentration. As such, the same procedure cannot be followed to obtain the LDF coefficient independently. Experiments on both test stand A and B were conducted using clay bound zeolite 5A pellets of

similar diameter. Considering that the mass transfer coefficient is in theory only a function of the adsorbent-adsorbate pair, the LDF coefficient obtained from stand A ($k_n = 2.1\times10^{-3}$ s^{-1}) is used to determine the axial dispersion coefficients for test stand B. Using this LDF coefficient, breakthrough simulations were run for test stand B while varying the axial dispersion from 1×10^{-7} m^2/s to 1 m^2/s in logarithmic steps (twenty steps per decade). The simulated concentration for each of these axial dispersion coefficients is compared with experimental data for the mixed concentration downstream of the bed. Figure 8a shows the breakthrough curve from the best-fit simulation (black line) and experimental measurements (red line) in test stand B, and Figure 8b shows the SSE as a function of axial dispersion coefficient, respectively. Concentration measurements in test stand B are taken at a sufficiently high temporal frequency to allow direct comparison with the simulation results when computing the SSE. Again, only data in the middle 50% of the concentration range are used for this calculation (indicated by the dashed blue horizontal lines in Figure 8a). The resulting plot of SSE over the range of axial dispersion values evaluated shows no clear minimum SSE in Figure 8b. Rather, the error asymptotically approaches a constant, minimum value as the axial dispersion coefficient tends toward zero, with the best fit to the experimental results being the lowest simulated value, $D_{ax} = 1\times10^{-7}$ m^2/s. This result indicates that axial mixing in test stand B is not dominated by channeling effects and the experiment is well represented by a plug-flow model. Furthermore, as the error remains relatively constant for all values of $D_{ax} \leq 2\times10^{-3}$ m^2/s, we can use the Edwards and Richardson[52] correlation for pellet-driven axial dispersion with good accuracy for test stand B. These calibrated LDF and axial dispersion coefficients are taken as the baseline model inputs for the uncertainty analysis performed.

Comparison of model to experiments

Using the calibrated LDF and the axial dispersion coefficients, we assess the model predictions for a case with all input parameters fixed at a set of baseline values. These model input parameters and their baseline values are given in Table 4 for test stands A and B. The parameters are subdivided into three categories: bed parameters, heat transfer coefficients, and adsorbent properties. The model predictions are assessed in terms of five different output performance metrics:

1. breakthrough time, t_b – the time when the concentration of adsorbate at the bed exit, c, first reaches 1% of the inlet concentration (*i.e.*, $c/c_0 \geq 0.01$);
2. stoichiometric breakthrough time, $\bar{t}_{stoich}$ – the time it would take to completely saturate the bed if there were no mass transport resistance, found via integration,

$$\bar{t}_{stoich} = \int_0^\infty \left(1 - \frac{c(t)}{c_0}\right) dt \ ; \tag{19}$$

3. total capacity, χ – the mass of CO_2 adsorbed by the zeolite 5A bed after the bed is saturated (*i.e.*, $c/c_0 \geq 0.99$);
4. time to reach maximum outlet temperature, $t(T_{g,max})$ – the time when the bed exit gas temperature reaches its maximum value;
5. maximum temperature rise, $\Delta T_{g,max}$ – the maximum temperature difference of the gas across the bed (*i.e.*, $T_g(z = L) - T_g(z = 0)$); and
6. mean temperature rise, $\Delta T_{g,mean}$ – the time-averaged temperature difference of the gas across the bed.

The model is run with the input values as given in Table 4 to obtain baseline output parameters for both test stands. These results are tabulated in Table 5. Figure 9 shows the breakthrough curve

from the baseline simulation (dashed line) alongside experimental measurements of the mixed downstream concentration for test stands A and B (panels a and b, respectively). The simulation breakthrough curve matches the experimental data very well. Test stand A takes approximately twice as long to break through (see solid green lines in Figure 9a and b). Given that both beds are subject to similar superficial velocities and bed void fractions (see Table 2), we attribute this difference in breakthrough time to the difference in bed length. For similar reasons, the stoichiometric breakthrough time of test stand A is greater than of test stand B (see dotted green lines in Figure 9a and b). The bed in test stand B is larger and thus holds more pellets and has a greater total capacity for holding CO_2. Normalizing the capacities of the two beds by the mass of adsorbent in each, we find that both beds hold approximately 5% CO_2 by mass at equilibrium. Figure 9 also shows the effluent temperature from the baseline simulation (dashed line) alongside experimental measurements of the mixed downstream concentration for test stand A and test stand B (panels c and d, respectively). The initial spike in the experimentally measured temperature of test stand A is attributed to N_2 adsorption. Recall that test stand A is kept in a helium environment prior to starting the breakthrough experiment. The introduction of nitrogen to the adsorption bed results in a slight rise in temperature as a minute quantity is adsorbed onto the zeolites; this phenomenon is not captured in our simulation results, which treat nitrogen as inert. Apart from this discrepancy in test stand A, the simulation predictions closely follow the initial temperature rise and match the maximum temperature to within one degree. The outlet temperature peaks sooner in test stand B than A, again due to the difference in bed length. Notably, the outlet temperature peaks in test stand B simultaneously with breakthrough. We attribute this to the very low axial dispersion in test stand B which closely mimics ideal plug-flow behavior. This close match also indicates that temperature gradient in the radial direction of the bed is small and thus

the overall temperature gradient, which is primarily axial, is well represented by the one-dimensional model.

Uncertainty analysis

We next perform an analysis of model uncertainty given the expected potential deviations from these baseline parameters as described in the *Model inputs* section. The percent change versus the baseline case is evaluated using the six performance metrics (defined under *Comparison of model to experiments*) for upper and lower bounding values of each model input parameter. These bounds are summarized in Table 6. Given the excellent agreement between baseline model and experiments, we consider this analysis as an approximation of uncertainty in the model predictions. The adsorbent conductivity and specific heat are excluded from this table because uncertainty values were not provided by the manufacturers, and also based on the results from a sensitivity analysis which showed that, at ±10% uncertainty, these parameters would have a negligible effect on the simulated performance[44].

Simulations were performed for all high and low bounding values included in Table 6. The percent changes in the performance metrics were then compared to the baseline case. Table 7 reports these relative percent changes in the breakthrough time, stoichiometric breakthrough time, and total bed capacity. The analysis reveals that (for both test stands) the greatest uncertainties in the effluent concentration come from three parameters: LDF coefficient, void fraction, and pellet density. In addition to these parameters, uncertainty in axial dispersion is also important for test stand A. This is because wall channeling due to the small pellet-to-canister diameter ratio in test stand A results in significant axial mixing, which is not captured by the empirical correlations used to predict axial dispersion, as these correlations only account for pellet-driven dispersion. Thus,

the baseline dispersion is almost an order of magnitude larger than the dispersion simulated for the uncertainty analysis.

Figure 10 shows the breakthrough curve of the four simulations for which the axial dispersion and the LDF coefficient were held at their upper or lower uncertainty bounds, in addition to the baseline results. As expected, it shows that the slope of the breakthrough curve increases as the LDF coefficient is increased from the baseline value, causing the bed to breakthrough earlier; decreasing the LDF has the opposite effect on breakthrough time. Simulations run using the upper and lower bounds of axial dispersion coefficient, D_{ax}, deviate significantly from the baseline in test stand A. Both cases show a similar steepening of the curve which causes the breakthrough time to increase. The deviation in test stand A is due to the extremely high experimentally measured D_{ax} that is an order of magnitude larger than even the upper uncertainty bound on D_{ax}. We note that Figure 10 shows negligible deviation from the baseline case in test stand B as D_{ax} is changed. This is consistent with the results of Knox[44], who found that it is important to accurately capture the effects of wall channeling in small-diameter, fixed adsorbent beds. The high axial dispersion, which we found by fitting to experimental data, decreased the breakthrough time by 24% compared to *ad hoc* empirical predictions in test stand A (Table 7). This significant change in breakthrough time directly impacts the adsorption efficiency of the bed. Table 7 also shows that varying either the LDF coefficient or the axial dispersion has no effect on the capacity, which is expected considering that these parameters govern only the kinetics (and not equilibrium characteristics) of adsorption. Finally, we note that the uncertainty for both the stoichiometric breakthrough time and total capacity is approximately 1% for both test stands due to the accuracy with which we can determine porosity and void fraction.

We also evaluated the impact of changing the model inputs on the three metrics quantifying the temperature of the gas stream leaving the bed. Both the composition and temperature of this effluent stream are of great interest in modeling multi-bed sorption systems, such as the CDRA and the next generation of four-bed molecular sieves (4BMS), because the effluent of one bed becomes the influent stream of the next. We choose the time at which the maximum outlet temperature is reached as a metric because it quantifies the time at which the thermal wave exits the bed (analogous to the breakthrough time for mass transport). The results are tabulated in Table 8. Evaluation of the temperature metrics shows that several parameters are important to the model uncertainty: LDF coefficient, axial dispersion, effective axial thermal conductivity, gas–canister heat transfer coefficient, and canister–insulation heat transfer coefficient. The effect of axial dispersion on temperature is only significant in test stand A due to the order-of-magnitude difference between the predicted axial dispersion and the baseline measured D_{ax} for stand A. The effect of varying LDF coefficient and effective axial thermal conductivity are similar for both test stands; the exit temperature metrics for both test stands follow the same trend and show similar order-of-magnitude changes. However, the effluent temperatures of test stands A and B were sensitive to different heat transfer coefficients. We attribute this to differences in canister material and thicknesses. Test stand A is constructed of a thin aluminum wall which has minimal thermal capacity and resistance; thus, heat easily flows through the canister wall and into the insulation. Conversely, test stand B has a thick, steel canister wall which acts as a large heat sink during the breakthrough process. Thus, test stand A was more strongly influenced by the canister-insulation heat transfer while test stand B was most strongly affected by the gas-canister heat transfer. It is important to note that the uncertainty bounds for the canister–insulation and insulation–ambient heat transfer coefficients were chosen to be extreme examples (*e.g.*, we vary $h_{can\text{-}ins}$ from 0 to ∞).

Even with this very large range of values, the effect on the temperature behavior only changed by a few percents compared to the baseline. This is due to the weak temperature gradients observed during adsorption which are only on the order of 10 K. We expect that the model predictions would be significantly more prone to error due to uncertain heat transfer coefficients when modeling temperature-assisted desorption (where the bed is heated to nearly 300ºC). For test stand A, the maximum temperature rise across the bed is also sensitive to the axial dispersion coefficient; again, this is due to the order-of-magnitude discrepancy of our experimentally measured axial dispersion from the expected range of D_{ax}. The mean temperature rise is proportional to the total energy transferred to the gas-phase during adsorption, which is simply proportional to the total mass of CO_2 adsorbed less the heat loss to ambient and absorbed by the thermal mass of the test stand. As the thermal mass of the bed is small, we see that uncertainty in the mean temperature rise across the bed is mainly influenced by heat loss through the lateral walls.

The effluent temperature of the simulation cases for which the temperature profile was most strongly affected by the uncertain parameter being evaluated is shown in Figure 11, along with the baseline case. Figure 11a shows that the time to reach the maximum outlet temperature remains largely unchanged for test stand A, while the maximum temperature rise across the bed is strongly influenced by the canister-insulation heat transfer coefficient; the same trend is seen in test stand B, but with the gas-canister heat transfer coefficient having the strong influence (Figure 11b). From Figure 11b we also see that the upper bound of the effective axial thermal conductivity causes a noticeable drop in the maximum effluent temperature compared with the baseline, while the lower bound has negligible effect. This is because the axial conduction in the baseline case is very low, much closer to the lower bound than the upper bound.

Conclusions

We performed an uncertainty analysis to understand the variation in predictions of a one-dimensional, fixed-bed adsorption model given expected potential deviations in several model input parameters including bed transport properties, heat transfer coefficients, and thermophysical adsorbent properties. The model was calibrated to experimental breakthrough data from two test stands of different lengths and pellet-to-bed diameter ratios. This work is the first documented validation of the calibration method proposed by Knox *et al.*[33]. We showed that the LDF extracted from centerline measurements in the smaller test stand A could be used to predict breakthrough in the larger test stand B yielding excellent agreement with experimental data. The uncertainty analysis was then performed for both test stands to which the model was calibrated by independently changing the model inputs between their lower and upper bounds of their predicted values. The model uncertainty was found by evaluating the resulting change in predicted performance metrics. Metrics such as the breakthrough time, total capacity, and time-averaged temperature rise across the bed were used to evaluate the model's uncertainty to these inputs for breakthrough of CO_2 on zeolite 5A in an N_2 carrier gas. These metrics were selected due to their importance when modeling multi-bed systems. Based on the breakthrough time and capacity, uncertainty in the LDF coefficient and axial dispersion were identified to be the greatest source of model uncertainty. Only two parameters had a notable effect on the stoichiometric breakthrough time or capacity—porosity and pellet density—though the uncertainty in the predicted stoichiometric breakthrough time and capacity were small (~1%). The uncertainty analysis further identified that it is important to accurately predict the axial dispersion coefficient accounting for dispersion effects beyond pellet-driven dispersion. As previously noted by Knox *et al.*[33], empirical prediction of this parameter can induce large errors in beds with small pellet-to-diameter ratio

(such as the small channels in a CDRA adsorbent core), due to a failure to account for wall-channeling effects. The analysis also indicated that it is vital to obtain sufficiently accurate measurements of pellet density and bed void fraction to which the performance is highly sensitive. As we transition from a traditional design-build-test approach to simulation-based design, we need a firm understanding of the sensitivities and uncertainties of our models. This work should aid in the design of life support systems for deep space exploration as engineers continue to push the limits of model-based design and optimization.

Acknowledgments

The first author acknowledges financial support from a National Aeronautics and Space Administration (NASA) Space Technology Research Fellowship (NSTRF grant #NNX13AL55H). We thank Robert F. Coker for his assistance and invaluable advice in setting up the one-dimensional adsorption model.

Notation

A	area, m^2
A_{fr}	free-flow area ($\pi d_{can,in}{}^2/4$), m^2
c	molar concentration, mol/m^3
c_p	specific heat capacity, J/(kg K)
d	diameter, m
$D_{eff,j}$	effective diffusivity of species *j* in the gas-phase mixture, $\left(1/D_{M,j}+1/D_{K,j}\right)^{-1}$, cm^2/sec
D_{jk}	binary diffusion coefficient of species *j* in species *k*, cm^2/sec
$D_{K,j}$	Knudsen diffusivity of species *j* in the gas-phase mixture, cm^2/sec
$D_{M,j}$	molecular diffusivity of species *j* in the gas-phase mixture, cm^2/sec
D_{ax}	axial dispersion coefficient, m^2/s
h	heat transfer coefficient, $W/(m^2 K)$
k	thermal conductivity, W/(m K)
k_n	linear-driving-force (LDF) mass transfer coefficient, 1/s
k_{eff}^0	effective axial thermal conductivity of a quiescent bed, W/(m K)
k_{eff}	effective axial thermal conductivity of bed with flow, W/(m K)
L	adsorbent bed length, m
M	molar mass, g/mol
p	pressure, kPa

q adsorbate concentration in the adsorbed phase, mol/m^3

q^* equilibrium adsorbed-phase concentration, mol/m^3

t time, s

t_b breakthrough time, s

$\bar{t}_{stoich}$ stoichiometric breakthrough time, s

T temperature, K

ΔT_g temperature change of gas across the bed, K

u_∞ superficial fluid velocity, m/s

u_i interstitial fluid velocity (u_∞ / ε), m/s

V volume, m^3

V_{bed} total bed volume ($\pi d_{can,in}{}^2 L/4$), m^3

$\dot{V}$ volumetric flow rate, SLPM (at 1 atm and 273.15 K)

z axial position, m

y_j mole fraction of species *j*, [mol/mol]

Greek symbols

β radial dispersion factor

ε void fraction of the adsorbent bed

λ isosteric heat of adsorption, J/mol

μ dynamic viscosity, kg/(m s)

ρ density, kg/m^3

ρ_{env}	pellet envelope density, kg/m^3
τ	tortuosity
χ	total capacity measured as mass of CO_2 adsorbed, g

Subscripts

0	inlet condition
amb	ambient
can	canister containing adsorbent
CO_2	carbon dioxide
g	gas-phase
init	initial
in	inner, inside
ins	insulation
max	maximum
mean	mean
out	outer, outside
p	pellet
s	adsorbent

Dimensionless groups

Nu	Nusselt number
Pe	Peclet number ($Re \times Pr$)
Pe_∞	Peclet number at infinite velocity
Pr	Prandlt number ($\mu c_p / k$)

Re_p pellet Reynolds number ($u_\infty d_p \rho_g / \mu_g$)

Sc_j Schmidt number of species j ($\mu_g / \rho_g D_j$)

References

(1) Do, D. D. *Adsorption Analysis: Equilibria and Kinetics*; Series on chemical engineering ; v. 2; Imperial College Press: London, England, 1998.

(2) Lo, I. M. C.; Alok, P. A. Computer Simulation of Activated Carbon Adsorption for Multi-Component Systems. *Environ. Int.* **1996**, *22* (2), 239–252.

(3) Farhadpour, F. A.; Bono, A. Sorptive Separation of Ethanol-Water Mixtures with a Bi-Dispersed Hydrophobic Molecular Sieve, Silicalite: Measurement and Theoretical Analysis of Column Dynamics. *Chem. Eng. Processing* **1996**, *35* (2), 157–168.

(4) Abdel-Jabbar, N.; Al-Asheh, S.; Hader, B. Modeling, Parametric Estimation, and Sensitivity Analysis for Copper Adsorption with Moss Packed-Bed. *Sep. Sci. Technol.* **2001**, *36* (13), 2811–2833.

(5) Ko, D. C. K.; Porter, J. F.; McKay, G. Film-Pore Diffusion Model for the Fixed-Bed Sorption of Copper and Cadmium Ions onto Bone Char. *Water Res* **2001**, *35* (16), 3876–3886.

(6) Gomez-Salazar, S.; Lee, J. S.; Heydweiller, J. C.; Tavlarides, L. L. Analysis of Cadmium Adsorption on Novel Organo-Ceramic Adsorbents with a Thiol Functionality. *Ind. Eng. Chem. Res.* **2003**, *42* (14), 3403–3412.

(7) Worch, E. Modelling the Solute Transport under Nonequilibrium Conditions on the Basis of Mass Transfer Equations. *J. Contam. Hydrol.* **2004**, *68* (1–2), 97–120.

(8) Chakraborty, S.; De, S.; DasGupta, S.; Basu, J. K. Adsorption Study for the Removal of a Basic Dye: Experimental and Modeling. *Chemosphere* **2005**, *58* (8), 1079–1086.

(9) Glover, T. G.; LeVan, M. D. Sensitivity Analysis of Adsorption Bed Behavior: Examination of Pulse Inputs and Layered-Bed Optimization. *Chem. Eng. Sci.* **2008**, *63* (8), 2086–2098.

(10) Lv, L.; Zhang, Y.; Wang, K.; Ray, A. K.; Zhao, X. S. Modeling of the Adsorption Breakthrough Behaviors of Pb2+ in a Fixed Bed of ETS-10 Adsorbent. *J. Colloid Interf. Sci.* **2008**, *325* (1), 57–63.

(11) Richard, D.; Delgado, N.; Schweich, D. Adsorption of Complex Phenolic Compounds on Active Charcoal: Breakthrough Curves. *Chem. Eng. J.* **2010**, *158* (2), 213–219.

(12) Abu-Lail, L.; Bergendahl, J. A.; Thompson, R. W. Mathematical Modeling of Chloroform Adsorption onto Fixed-Bed Columns of Highly Siliceous Granular Zeolites. *Environ. Prog. Sustain. Energy* **2012**, *31* (4), 591–596.

(13) Likozar, B.; Senica, D.; Pavko, A. Interpretation of Experimental Results for Vancomycin Adsorption on Polymeric Resins in a Fixed Bed Column by Mathematical Modeling with Independently Estimated Parameters. *Ind. Eng. Chem. Res.* **2013**, *52* (26), 9247–9258.

(14) Nur, T.; Shim, W. G.; Johir, M. A. H.; Vigneswaran, S.; Kandasamy, J. Modelling of Phosphorus Removal by Ion-Exchange Resin (Purolite FerrIX A33E) in Fixed-Bed Column Experiments. *Desalin. Water Treat.* **2014**, *52* (4–6), 784–790.

(15) Gupta, K. N.; Rao, N. J.; Agarwal, G. K. Gaseous Phase Adsorption of Volatile Organic Compounds on Granular Activated Carbon. *Chem. Eng. Commun.* **2015**, *202* (3), 384–401.
(16) Davila-Guzman, N. E.; Cerino-Córdova, F. J.; Loredo-Cancino, M.; Rangel-Mendez, J. R.; Gómez-González, R.; Soto-Regalado, E. Studies of Adsorption of Heavy Metals onto Spent Coffee Ground: Equilibrium, Regeneration, and Dynamic Performance in a Fixed-Bed Column. *Int. J. Chem. Eng.* **2016**, *2016*.
(17) Shao, Y.; Chen, H. Adsorption Kinetics of P-Nitrophenol (PNP) on Coal-Based Activated Carbon: Experimental and Simulation. *Desalin. Water Treat.* **2016**, *57* (31), 14496–14505.
(18) Chahbani, M. H.; Tondeur, D. Mass Transfer Kinetics in Pressure Swing Adsorption. *Sep. Purif. Technol.* **2000**, *20* (2–3), 185–196.
(19) Onyestyák, G.; Shen, D.; Rees, L. V. C. Frequency-Response Studies of CO2 Diffusion in Commercial 5A Powders and Pellets. *Microporous Materials* **1996**, *5* (5), 279–288.
(20) Hartzog, D. G.; Sircar, S. Sensitivity of PSA Process Performance to Input Variables. *Adsorption* **1995**, *1* (2), 133–151.
(21) Ratto, M.; Lodi, G.; Costa, P. Sensitivity Analysis of a Fixed-Bed Gas-Solid TSA: The Problem of Design with Uncertain Models. *Sep. Technol.* **1996**, *6* (4), 235–245.
(22) Yu, Z.; Peldszus, S.; Huck, P. M. Adsorption of Selected Pharmaceuticals and an Endocrine Disrupting Compound by Granular Activated Carbon. 2. Model Prediction. *Environ. Sci. Technol.* **2009**, *43* (5), 1474–1479.
(23) Reijers, H. T. J.; Boon, J.; Elzinga, G. D.; Cobden, P. D.; Haije, W. G.; van den Brink, R. W. Modeling Study of the Sorption-Enhanced Reaction Process for CO2 Capture. I. Model Development and Validation. *Ind. Eng. Chem. Res.* **2009**, *48* (15), 6966–6974.
(24) Lu, Y.; He, J.; Wu, L.; Luo, G. Relationship between Breakthrough Curve and Adsorption Isotherm of Ca(II) Imprinted Chitosan Microspheres for Metal Adsorption. *Chin. J. Chem. Eng.* **2016**, *24* (2), 323–329.
(25) Aguilera, P. G.; Gutiérrez Ortiz, F. J. Prediction of Fixed-Bed Breakthrough Curves for H2S Adsorption from Biogas: Importance of Axial Dispersion for Design. *Chem. Eng. J.* **2016**, *289*, 93–98.
(26) Zheng, M.; Xu, C.; Hu, H.; Ye, Z.; Chen, X. A Modified Homogeneous Surface Diffusion Model for the Fixed-Bed Adsorption of 4,6-DMDBT on Ag–CeOx/TiO2–SiO2. *RSC Adv.* **2016**, *6* (114), 112899–112907.
(27) Sircar, S.; Hufton, J. R. Why Does the Linear Driving Force Model for Adsorption Kinetics Work? *Adsorption* **2000**, *6* (2), 137–147.
(28) Shafeeyan, M. S.; Wan Daud, W. M. A.; Shamiri, A. A Review of Mathematical Modeling of Fixed-Bed Columns for Carbon Dioxide Adsorption. *Chemical Engineering Research and Design* **2014**, *92* (5), 961–988.
(29) Reijers, H. T. J.; Boon, J.; Elzinga, G. D.; Cobden, P. D.; Haije, W. G.; Brink, R. W. van den. Modeling Study of the Sorption-Enhanced Reaction Process for CO2 Capture. II. Application to Steam-Methane Reforming. *Ind. Eng. Chem. Res.* **2009**, *48* (15), 6975–6982.
(30) Naja, G.; Volesky, B. Optimization of a Biosorption Column Performance. *Environ. Sci. Technol.* **2008**, *42* (15), 5622–5629.
(31) Maring, B. J.; Webley, P. A. A New Simplified Pressure/Vacuum Swing Adsorption Model for Rapid Adsorbent Screening for CO2 Capture Applications. *Int. J. Greenh. Gas Con.* **2013**, *15*, 16–31.
(32) Kalyanaraman, J.; Kawajiri, Y.; Realff, M. J. Bayesian Estimation, Uncertainty Propagation and Design of Experiments for CO2 Adsorption on Amine Sorbents. In *Proceedings of the*

8th International Conference on Foundations of Computer-Aided Process Design; Eden, M. R., Siirola, J. D., Towler, G. P., Eds.; Cle Elum, WA, 2014; pp 345–350.
(33) Knox, J. C.; Ebner, A. D.; LeVan, M. D.; Coker, R. F.; Ritter, J. A. Limitations of Breakthrough Curve Analysis in Fixed-Bed Adsorption. *Ind. Eng. Chem. Res.* **2016**, *55* (16), 4734–4748.
(34) Borina, B.; Pavko, A. Adsorption of Vancomycin on Amberlite XAD-16 in a Packed Bed Column. *Chem. Biochem. Eng. Q.* **2009**, *23* (4), 479–483.
(35) Delgado, J. M. P. Q. A Critical Review of Dispersion in Packed Beds. *Heat Mass Transfer* **2006**, *42* (4), 279–310.
(36) Delgado, J. M. P. Q. Longitudinal and Transverse Dispersion in Porous Media. *Chem. Eng. Res. Des.* **2007**, *85* (9), 1245–1252.
(37) Vortmeyer, D.; Winter, R. P. Die Bedeutung Der Strömungsverteilung Für Die Modellierung von Chemischen Festbettreaktoren Bei Höheren Reynolds-Zahlen Und Ausgedehnten Reaktionszonen. *Chemie Ingenieur Technik 55* (12), 950–951.
(38) Vortmeyer, D.; Michael, K. The Effect of Non-Uniform Flow Distribution on Concentration Profiles and Breakthrough Curves of Fixed Bed Adsorbers. *Chemical Engineering Science* **1985**, *40* (11), 2135–2138.
(39) Augier, F.; Laroche, C.; Brehon, E. Application of Computational Fluid Dynamics to Fixed Bed Adsorption Calculations: Effect of Hydrodynamics at Laboratory and Industrial Scale. *Separation and Purification Technology* **2008**, *63* (2), 466–474.
(40) Sircar, S.; Kumar, R.; Anselmo, K. J. Effects of Column Nonisothermality or Nonadiabaticity on the Adsorption Breakthrough Curves. *Ind. Eng. Chem. Proc. Des. Dev.* **1983**, *22* (1), 10–15.
(41) Delage, F.; Pré, P.; Le Cloirec, P. Mass Transfer and Warming during Adsorption of High Concentrations of VOCs on an Activated Carbon Bed: Experimental and Theoretical Analysis. *Environ. Sci. Technol.* **2000**, *34* (22), 4816–4821.
(42) Sircar, S. Influence of Gas-Solid Heat Transfer on Rapid PSA. *Adsorption* **2005**, *11* (1), 509–513.
(43) Walton, K. S.; LeVan, M. D. Effect of Energy Balance Approximations on Simulation of Fixed-Bed Adsorption. *Ind. Eng. Chem. Res.* **2005**, *44* (19), 7474–7480.
(44) Son, K. N.; Weibel, J. A.; Garimella, S. V.; Knox, J. C. Calibration and Sensitivity of a Fixed-Bed Adsorption Model for Atmosphere Revitalization in Space. In *Proceedings of the 47th International Conference on Environmental Systems*; Charleston, South Carolina, 2017; p 173.
(45) *Human Exploration and Operations (HEO) Mission Directorate*; NASA, 2012.
(46) *2014 Strategic Plan*; NASA, 2014; pp 11–15.
(47) Coker, R.; Knox, J. Predictive Modeling of the CDRA 4BMS. In *Proceedings of the 46th International Conference on Environmental Systems*; Vienna, Austria, 2016.
(48) Knox, J.; Coker, R.; Howard, D.; Peters, W.; Watson, D.; Cmarik, G.; Miller, L. Development of Carbon Dioxide Removal Systems for Advanced Exploration Systems 2015-2016. In *Proceedings of the 46th International Conference on Environmental Systems*; Vienna, Austria, 2016.
(49) Knox, J. C. Predictive Simulation of Gas Adsorption in Fixed Beds and Limitations Due to the Ill-Posed Danckwerts Boundary Condition. dissertation, The University of Alabama in Huntsville: Huntsville, AL, 2016.

(50) Son, K. N.; Gomez, C.; Paragon, M.; Knox, J. C. Experimental Validation of Vacuum Desorption in 1-D Model of CO2 Removal. In *Proceedings of the 46th International Conference on Environmental Systems*; Vienna, Austria, 2016.
(51) Glueckauf, E.; Coates, J. I. Theory of Chromatography; the Influence of Incomplete Equilibrium on the Front Boundary of Chromatograms and on the Effectiveness of Separation. *J. Chem. Soc.* **1947**, 1315–1321.
(52) Edwards, M. F.; Richardson, J. F. Gas Dispersion in Packed Beds. *Chem. Eng. Sci.* **1968**, *23* (2), 109–123.
(53) *Material Library User's Guide*; COMSOL Multiphysics®, ver. 5.2a; COMSOL AB: Stockholm, SE.
(54) Wakao, N.; Kaguei, S.; Funazkri, T. Effect of Fluid Dispersion Coefficients on Particle-to-Fluid Heat Transfer Coefficients in Packed Beds. *Chem. Eng. Sci.* **1979**, *34* (3), 325–336.
(55) Li, C.-H.; Finlayson, B. A. Heat Transfer in Packed Beds—a Reevaluation. *Chem. Eng. Sci.* **1976**, *32* (9), 1055–1066.
(56) Yagi, S.; Kunii, D.; Wakao, N. Studies on Axial Effective Thermal Conductivities in Packed Beds. *AIChE J.* **1960**, *6* (4), 543–546.
(57) Krupiczka, R. Analysis of Thermal Conductivity in Granular Materials. *Int. Chem. Eng.* **1967**, *7* (1), 122–144.
(58) Langer, G.; Roethe, A.; Roethe, K.-P.; Gelbin, D. Heat and Mass Transfer in Packed Beds—III. Axial Mass Dispersion. *Int. J. Heat Mass Transf.* **1978**, *21* (6), 751–759.
(59) Fairbanks, D. F.; Wilke, C. R. Diffusion Coefficients in Multicomponent Gas Mixtures. *Ind. Eng. Chem.* **1950**, *42* (3), 471–475.
(60) Hirschfelder, J. O.; Curtiss, C. F.; Bird, R. B. *The Molecular Theory of Gases and Liquids*; Wiley-Interscience: London, England, 1964.
(61) Toth, J. State Equations of the Solid Gas Interface Layer. *Acta Chim. Acad. Sci. Hung.* **1971**, *69* (3), 311–317.
(62) Wang, Y.; LeVan, M. D. Adsorption Equilibrium of Carbon Dioxide and Water Vapor on Zeolites 5A and 13X and Silica Gel: Pure Components. *J. Chem. Eng. Data* **2009**, *54* (10), 2839–2844.
(63) Wakao, N.; Kagei, S. *Heat and Mass Transfer in Packed Beds*; Taylor & Francis: New York, NY, 1982.
(64) Bradshaw, A.; Johnson, A.; Mclachlan, N.; Chiu, Y. Heat Transfer between Air and Nitrogen and Packed Beds of Non-Reacting Solids. *Trans. Inst. Chem. Eng.* **1970**, *48* (3), T77–T84.
(65) De Acetis, J.; Thodos, G. Mass and Heat Transfer in Flow of Gases through Spherical Packings. *Ind. Eng. Chem.* **1960**, *52* (12), 1003–1006.
(66) Galloway, L. R.; Komarnicky, W.; Epstein, N. Effect of Configuration on Mass and Heat Transfer in Beds of Stacked Spheres. *Can. J. Chem. Eng.* **1957**, *35* (4), 139–150.
(67) Goss, M. J.; Turner, G. A. Simultaneous Computation of Heat Transfer and Dispersion Coefficients and Thermal Conductivity Value in a Packed Bed of Spheres: II. Technique of Computing Numerical Values. *AIChE J.* **1971**, *17* (3), 590–592.
(68) Handley, D.; Heggs, P.J. Momentum and Heat Transfer Mechanisms in Regular Shaped Packings. *Trans. Inst. Chem. Eng.* **1968**, *46*, T251–T264.
(69) Malling, G. F.; Thodos, G. Analogy between Mass and Heat Transfer in Beds of Spheres: Contributions Due to End Effects. *Int. J. Heat Mass Transf.* **1967**, *10* (4), 489–492.

(70) McConnachie, J. T. L.; Thodos, G. Transfer Processes in the Flow of Gases through Packed and Distended Beds of Spheres. *AIChE J.* **1963**, *9* (1), 60–64.
(71) Satterfield, C.; Resnick, H.; Wentworth, R. Simultaneous Heat and Mass Transfer in a Diffusion-Controlled Chemical Reaction. *Chem. Eng. Prog.* **1954**, *50* (9), 460–466.
(72) Sen Gupta, A.; Thodos, G. Direct Analogy between Mass and Heat Transfer to Beds of Spheres. *AIChE J.* **1963**, *9* (6), 751–754.
(73) Turner, G. A.; Otten, L. Values of Thermal (and Other) Parameters in Packed Beds. *Ind. Eng. Chem. Proc. Des. Dev.* **1973**, *12* (4), 417–424.
(74) Wilke, C. R.; Hougen, O. Mass Transfer in the Flow of Gases through Granular Solids Extended to Low Modified Reynolds Numbers. *Trans. Am. Inst. Chem. Eng.* **1945**, *41* (4), 445–451.
(75) Yagi, S.; Wakao, N. Heat and Mass Transfer from Wall to Fluid in Packed Beds. *AIChE J.* **1959**, *5* (1), 79–85.
(76) Kunii, D.; Suzuki, M.; Ono, N. Heat Transfer from Wall Surface to Packed Beds at High Reynolds Number. *J. Chem. Eng. Jpn.* **1968**, *1* (1), 21–26.
(77) McHenry, K. W.; Wilhelm, R. H. Axial Mixing of Binary Gas Mixtures Flowing in a Random Bed of Spheres. *AIChE J.* **1957**, *3* (1), 83–91.
(78) Carberry, J. J.; Bretton, R. H. Axial Dispersion of Mass in Flow through Fixed Beds. *AIChE J.* **1958**, *4* (3), 367–375.
(79) Blackwell, R. J.; Rayne, R. J.; Terry, W. M. Factors Influencing the Efficiency of Miscible Displacement. *J. Petrol. Technol.* **1959**, *217*, 9.
(80) Perkins, T. K.; Johnston, O. C. A Review of Diffusion and Dispersion in Porous Media. *Soc. Petrol. Eng. J.* **1963**, *3* (1), 70–84.
(81) Sinclair, R. J.; Potter, O. E. The Dispersion of Gas in Flow through a Bed of Packed Solids. *Trans. Inst. Chem. Eng.* **1965**, *43*, 3–9.
(82) Gunn, D. J.; Pryce, C. Dispersion in Packed Beds. *Trans. Inst. Chem. Eng.* **1969**, *47* (10), t341–t350.
(83) Johnson, G. W.; Kapner, R. S. The Dependence of Axial Dispersion on Non-Uniform Flows in Beds of Uniform Packing. *Chem. Eng. Sci.* **1990**, *45* (11), 3329–3339.
(84) Scott, D. S.; Lee, W.; Papa, J. The Measurement of Transport Coefficients in Gas-Solid Heterogeneous Reactions. *Chem. Eng. Sci.* **1974**, *29* (11), 2155–2167.
(85) Wicke, E. Significance of molecular diffusion for chromatographic procedures. *Ber. Bunsen-Ges. Phys. Chem. Chem. Phys.* **1973**, *77* (3), 160–171.
(86) Özgümüş, T.; Mobedi, M.; Özkol, Ü.; Nakayama, A. Thermal Dispersion in Porous Media—A Review on the Experimental Studies for Packed Beds. *Appl. Mech. Rev* **2013**, *65* (3), 031001.
(87) Kunii, D.; Smith, J. M. Heat Transfer Characteristics of Porous Rocks: II. Thermal Conductivities of Unconsolidated Particles with Flowing Fluids. *AIChE J.* **1961**, *7* (1), 29–34.
(88) Votruba, J.; Hlaváček, V.; Marek, M. Packed Bed Axial Thermal Conductivity. *Chem. Eng. Sci.* **1972**, *27* (10), 1845–1851.
(89) Gunn, D. J.; De Souza, J. F. C. Heat Transfer and Axial Dispersion in Packed Beds. *Chem. Eng. Sci.* **1974**, *29* (6), 1363–1371.
(90) Gunn, D. J.; Khalid, M. Thermal Dispersion and Wall Heat Transfer in Packed Beds. *Chem. Eng. Sci.* **1975**, *30* (2), 261–267.

(91) Vortmeyer, D.; Adam, W. Steady-State Measurements and Analytical Correlations of Axial Effective Thermal Conductivities in Packed Beds at Low Gas Flow Rates. *Int J Heat Mass Transf* **1984**, *27* (9), 1465–1472.
(92) Incropera, F. P.; DeWitt, D. P.; Bergman, T. L.; Lavine, A. S. *Fundamentals of Heat and Mass Transfer*, 6th edition.; John Wiley & Sons: Hoboken, NJ, 2006.
(93) *COMSOL Multiphysics®*; COMSOL AB: Stockholm, SE, 2016.
(94) *Adsorbents for Process Applications*; Grace Davison, W. R. Grace & Co.: Columbia, MD, 2010.
(95) Kay, R.; Pancho, D. *Evaluation of Alternative Desiccants and Adsorbents for the Desiccant/Adsorbent Bed*; 12–77742, CAGE 70210; Honeywell, 2013.
(96) *Q-Fiber® Felt Data Sheet*; HPI-25 4-08; Johns Manville: Denver, CO, 2008.
(97) *Datasheet Flexible Min-K®*; 6-14–120; Morgan Advanced Materials, 2013.
(98) *Physical Properties of Pyropel® Insulation*; Albany International: Rochester, NH.

Figures

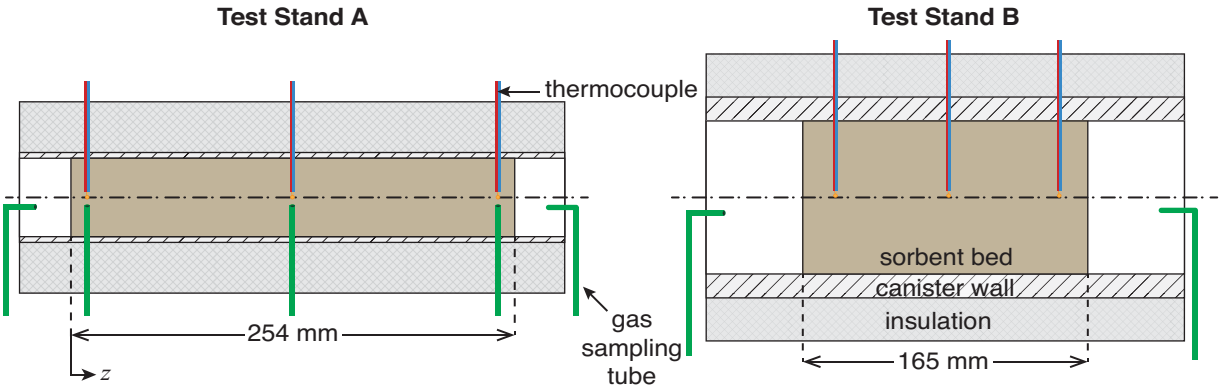

Figure 1. Cross-sectional views of the cylindrical canister and adsorbent bed for test stand A and test stand B, showing the axial locations of intra-bed temperature and CO_2 sensors. Note that the inlet and outlet gas sampling tubes are physically located far upstream and downstream respectively of the adsorbent.

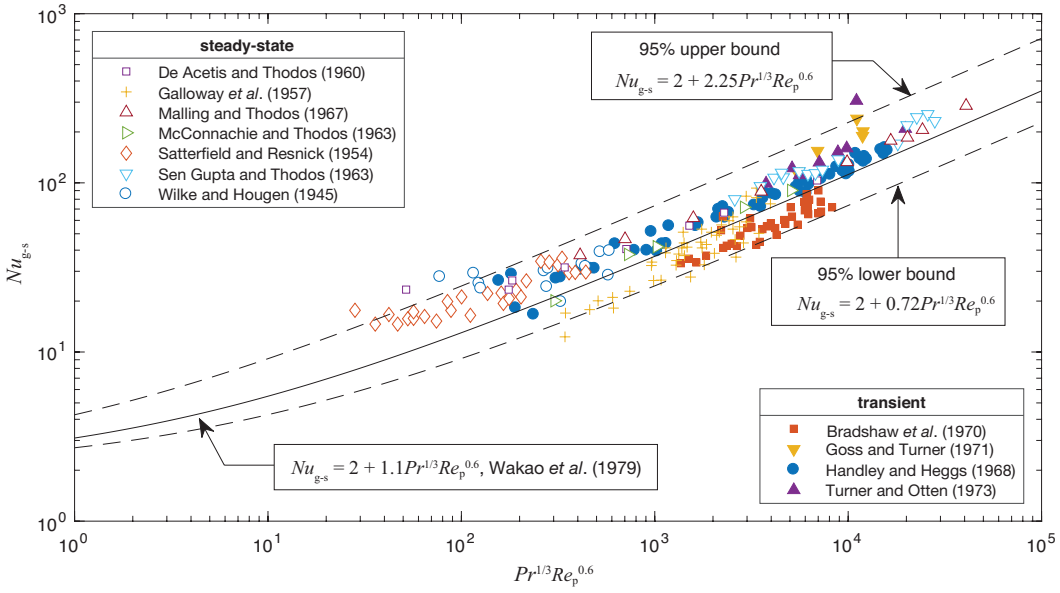

Figure 2. Experimental measurements[64–74] of interfacial gas-adsorbent Nusselt number compared with the correlation of Wakao *et al.*[54] (solid line) and uncertainty bounds (dashed lines) encompassing 95% of data.

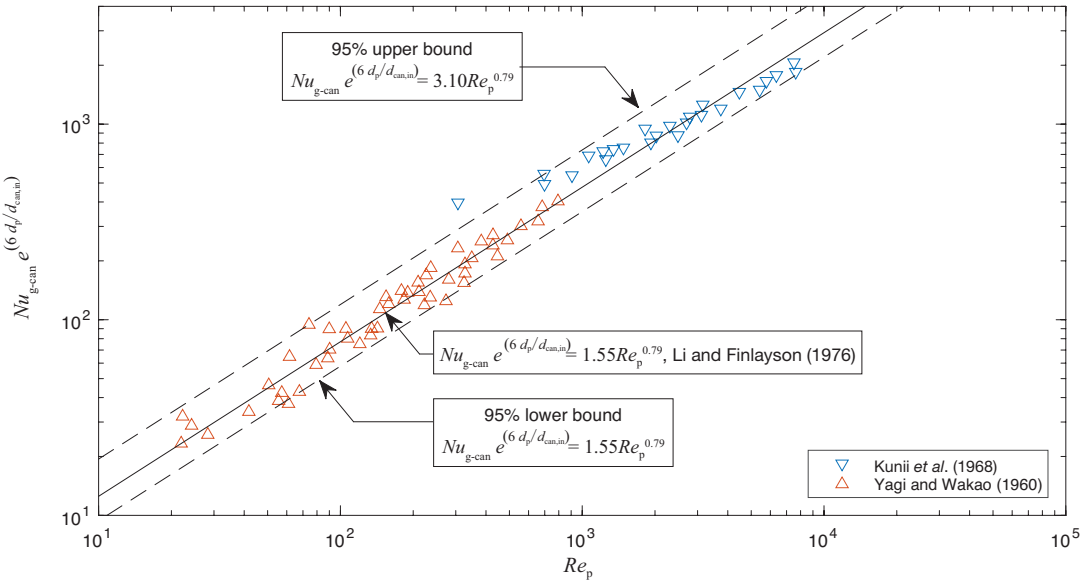

Figure 3. Experimental measurements[75,76] of gas-canister Nusselt number compared with the correlation of Li and Finlayson[55] (solid line) and uncertainty bounds (dashed lines) encompassing 95% of data.

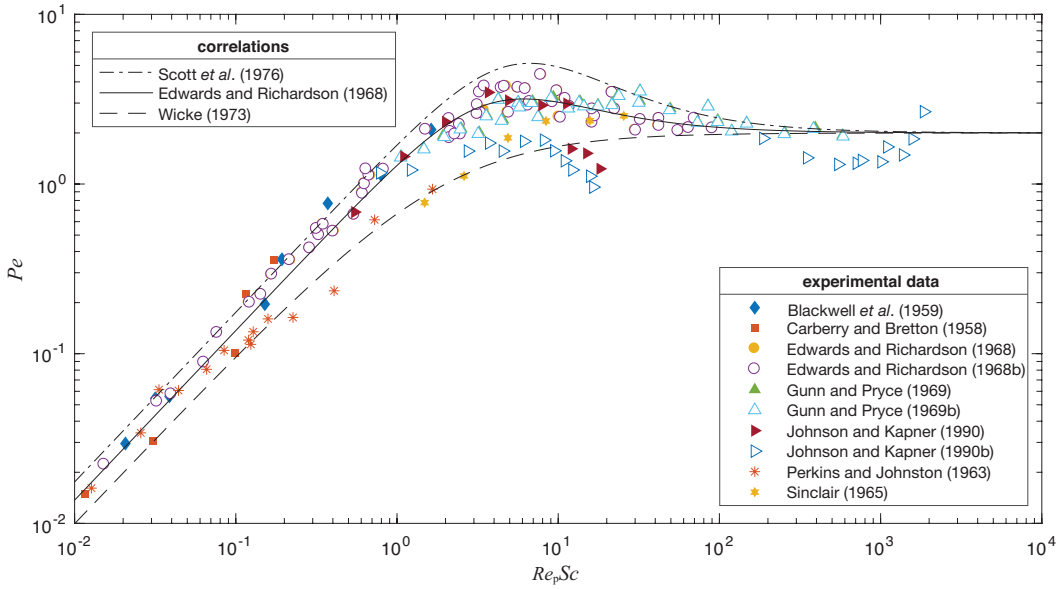

Figure 4. Experimental measurements[52,77–83] of axial dispersion of gases through fixed beds of spherical particles compared with the correlation of Edwards and Richardson[52] (solid line). Upper and lower uncertainty bounds on D_{ax} are estimated from the correlations of Scott *et al.*[84] and Wicke[85], respectively.

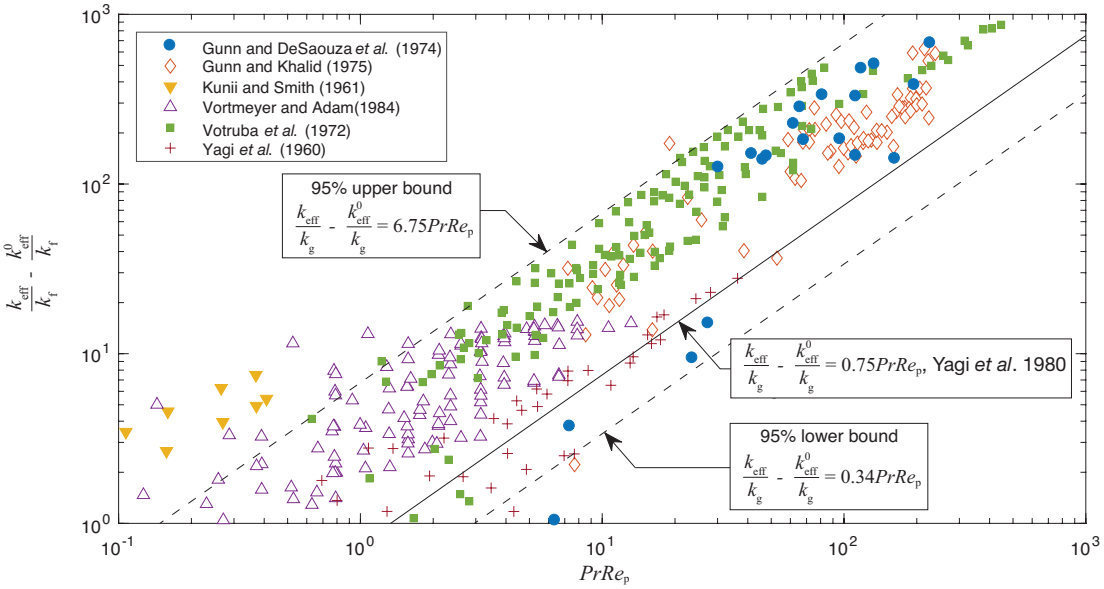

Figure 5. Experimental measurements[56,87–91] of effective axial thermal conductivity of a fixed bed of spherical particles with gas flow compared with the correlation of Yagi *et al.*[56] (solid line) and uncertainty bounds (dashed lines) encompassing 95% of data.

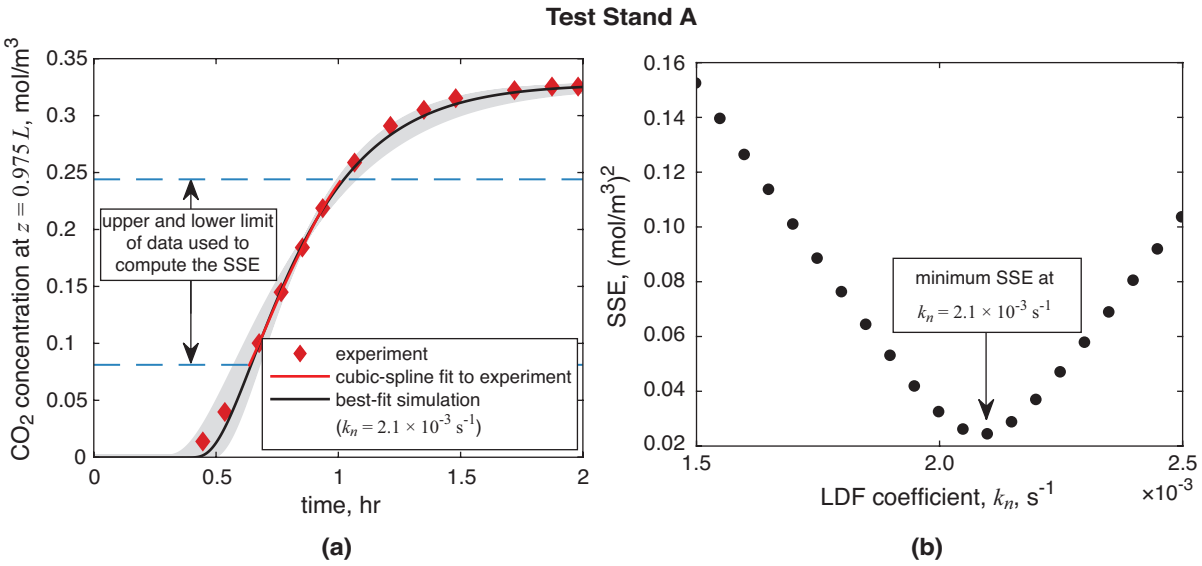

Figure 6. Calibration of LDF in test stand A: (a) model predictions shown alongside experimental measurements of exit concentration at 97.5% of the bed length for CO_2 breakthrough, and (b) the sum of squared errors (SSE) between the model prediction and cubic-spline fit to the experimental data as a function of LDF coefficient. The gray region in (a) marks the span of the simulated breakthrough curves for the range of LDF coefficients in (b). (D_{ax} = 1.13×10^{-3} m^2/s).

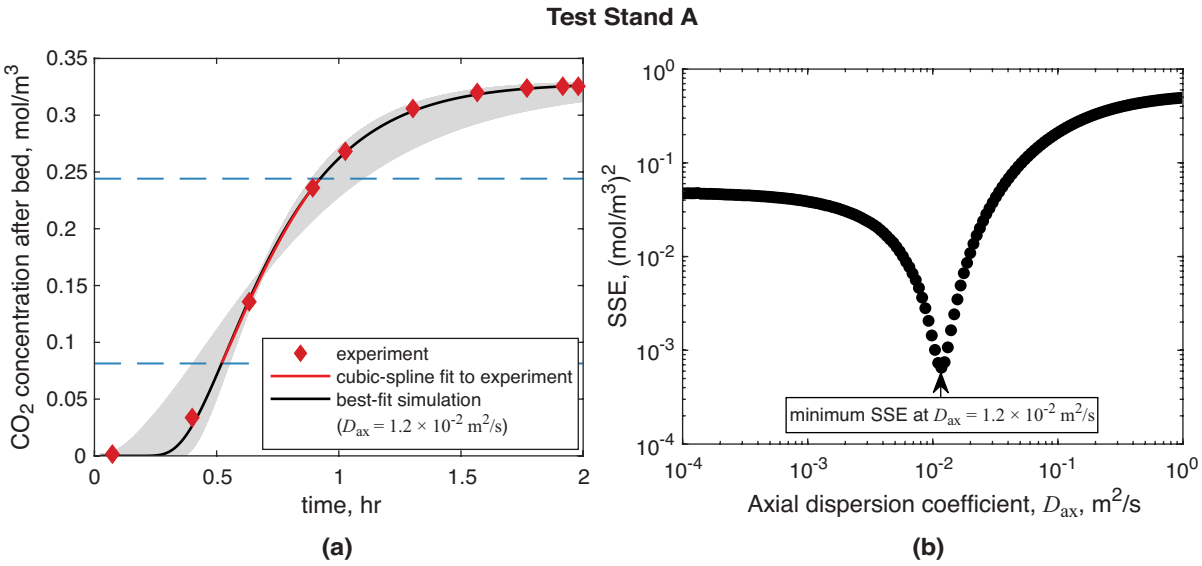

Figure 7. Calibration of D_{ax} in test stand A: (a) model predictions shown alongside experimental measurements of mixed concentration far downstream of the bed for CO_2 breakthrough, and (b) the SSE between the model prediction and cubic-spline fit to the experimental data as a function of D_{ax}. The gray region in (a) marks the span of the simulated breakthrough curves for the D_{ax} values simulated in (b). ($k_n = 2.1\times10^{-3}$ s^{-1}).

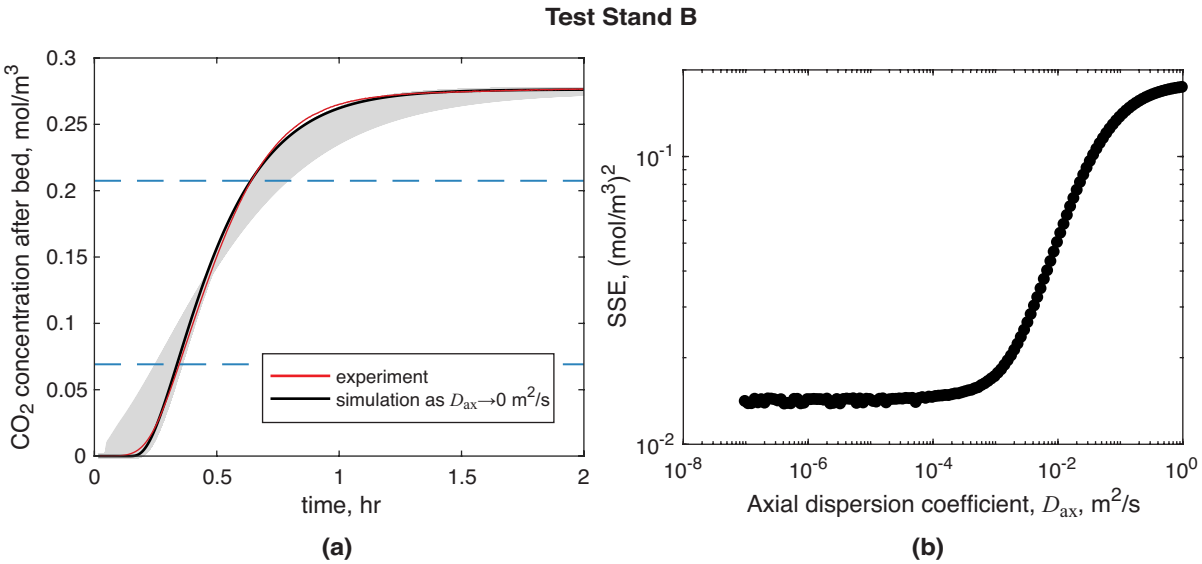

Figure 8. Calibration of D_{ax} in test stand B: (a) model predictions shown alongside experimental measurements of mixed concentration far downstream of the bed for CO_2 breakthrough, and (b) the SSE between the model prediction and the experimental data as a function of D_{ax}. The gray region in (a) marks the span of the simulated breakthrough curves for the D_{ax} values simulated in (b). ($k_n = 2.1\times10^{-3}$ s^{-1}).

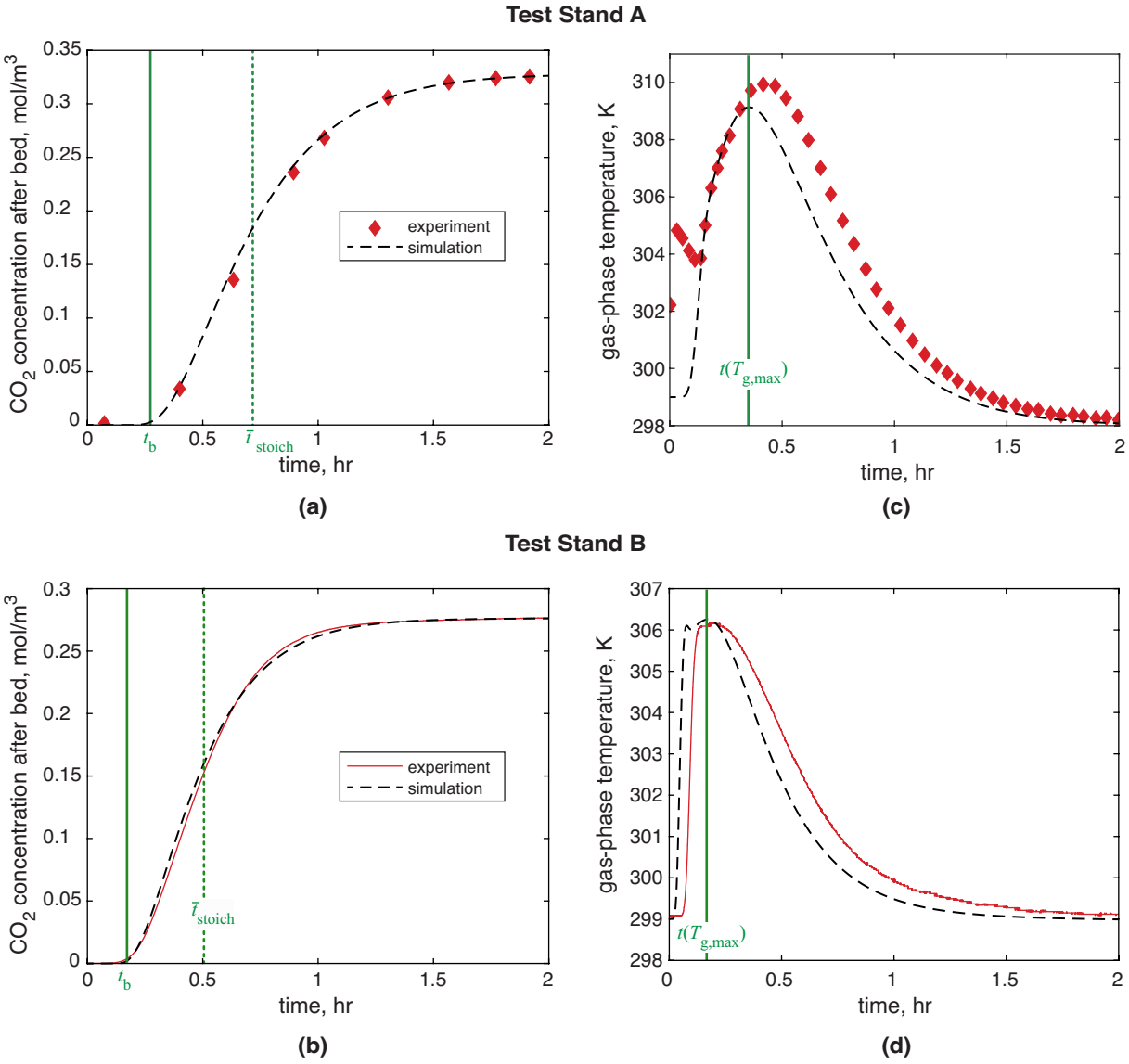

Figure 9. Comparison of baseline simulation and experimental data for test stand A (top) and test stand B (bottom). Left panels (a, b) show breakthrough curves and right panels (c, d) show exit temperature. All values are for mixed, downstream measurements.

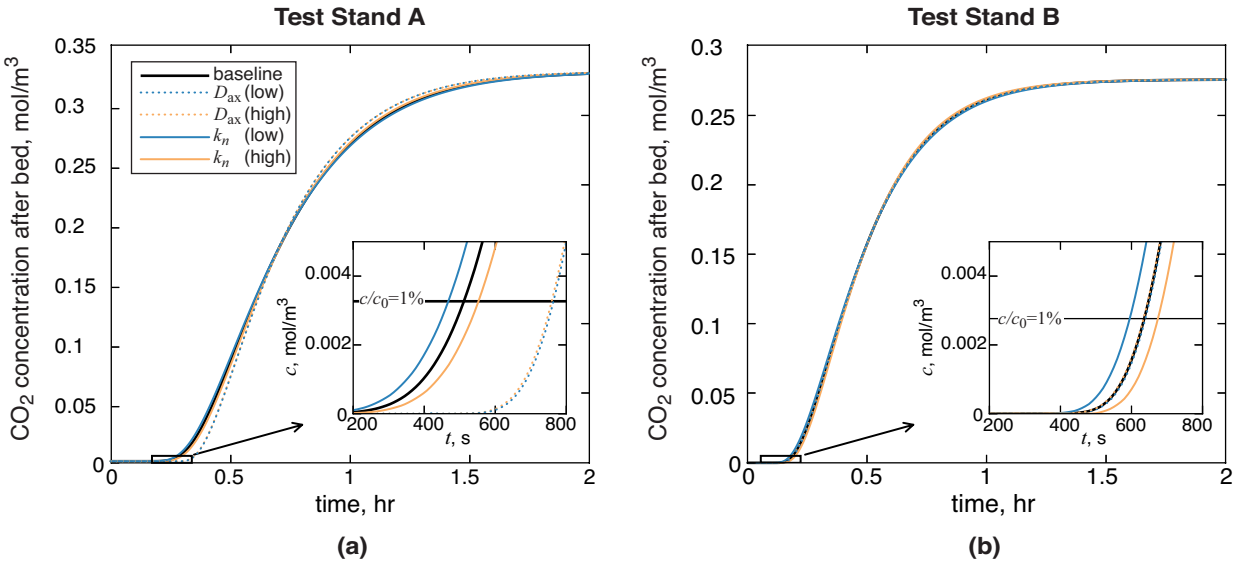

Figure 10. For test stand A (a) and test stand B (b): breakthrough curve for the baseline simulation input parameters compared with four simulations where either the LDF coefficient or the axial dispersion coefficient, were set to their upper or lower bound given in Table 6. The zoomed-in inset shows the time where the outlet concentration curve crosses the breakthrough point ($c/c_0 = 1\%$), *i.e.*, the breakthrough time.

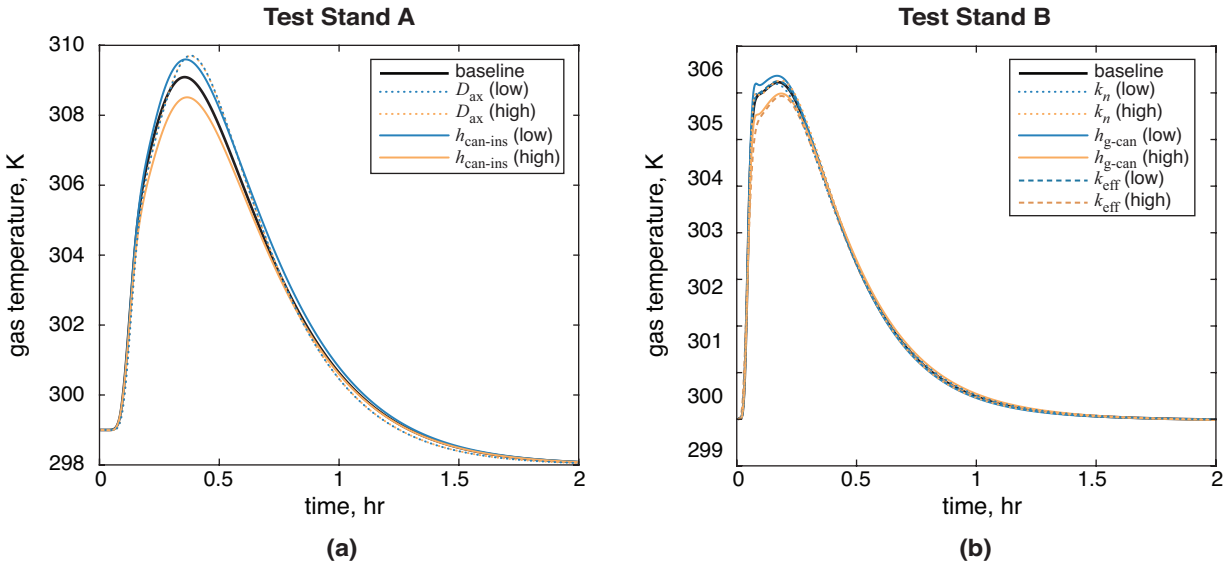

Figure 11. For test stand A (a) and test stand B (b): temperature of effluent for baseline simulation inputs compared with simulations where one of several input parameters were set to their upper or lower bound given in Table 6.

Tables

Table 1. Dimensions and physical properties of the test stand A[33] and test stand B[50].

		Test stand A	Test stand B
bed length, L, m		0.254	0.165
void fraction, ε		0.35	0.35
inner canister diameter, $d_{can,in}$, mm		47.6	93.6
adsorbent:	material	Grace Davidson grade 522[94]	UOP RK-38[95]
	mean pellet diameter, d_p, mm	2.32	2.1
	conductivity, k_s, W/(m K)	0.152	0.144
	heat capacity, $c_{p,s}$, J/(kg K)	920	650
	pellet envelope density, ρ_{env}, kg/m^3	1180	1179
canister:	material	stainless steel	aluminum
	thickness, t_{can}, mm	1.59	10.3
	conductivity, k_{can}, W/(m K)	14.2	205
	heat capacity, $c_{p,can}$, J/(kg K)	475	902
	density, ρ_{can}, kg/m^3	7833	2712
insulation:	material	Q-fiber®[96] and min-K®[97]	Pyropel® LD-6[98]
	thickness, t_{ins}, mm	25.4	15.9
	conductivity, k_{ins}, W/(m K)	0.038	0.032
	heat capacity, $c_{p,ins}$, J/(kg K)	747	747
	density, ρ_{ins}, kg/m^3	88	100

Table 2. Inlet and initial conditions for breakthrough of CO_2 on zeolite in test stands A[33] and B[50].

operational parameter	**Test stand A**	**Test stand B**
volumetric flow rate, $\dot{V}$, SLPM	28.3	132
inlet temperature, $T_{g,in}$, K	298	299
initial temperature, T_{init}, K	299	299
ambient temperature, T_{amb}, K	298	297
inlet total pressure, $p_{g,in}$, kPa	106	126
inlet CO_2 partial pressure, $p_{CO_2,in}$, kPa	0.816	0.689

Table 3. Toth equilibrium adsorption isotherm parameters for CO_2 on Zeolite 5A[62].

a_0, mol/(kg kPa)	b_0, kPa^{-1}	E, K	t_0	c, K
9.875×10^{-7}	6.761×10^{-8}	5625	0.27	-20.02

Table 4. Baseline values of the model input parameters varied in the uncertainty analysis.

model input parameter	**test stand A**	**test stand B**
linear-driving-force coefficient, k_n, s^{-1}	2.1×10^{-3}	2.1×10^{-3}
axial dispersion (eq 13), D_{ax}, m^2/s	1.20×10^{-2}	1.13×10^{-3}
effective axial thermal conductivity (eq 11), k_{eff}, W/(m K)	0.673	0.726
void fraction, ε	0.35	0.35
gas-adsorbent heat transfer coefficient (eq 9), $h_{g\text{-}s}$, $W/(m^2K)$	128	148
gas-canister heat transfer coefficient (eq 10), $h_{g\text{-}can}$, $W/(m^2K)$	16.9	10.8
canister-insulation heat transfer coefficient, $h_{can\text{-}ins}$, $W/(m^2K)$	3	3
insulation-ambient heat transfer coefficient, $h_{ins\text{-}amb}$, $W/(m^2K)$	3	3
adsorbent envelope density, ρ_{env}, kg/m^3	1180	1179
adsorbent thermal conductivity, k_s, W/(m K)	0.152	0.144
adsorbent specific heat, $c_{p,s}$, J/(kg K)	920	650

Table 5. Output metrics for the baseline simulation and experimental results.

	test stand A		test stand B	
output metrics	**simulation**	**experiment**	**simulation**	**experiment**
breakthrough time, t_b, s	1000	N/A*	630	580
stoichiometric breakthrough time, $\bar{t}_{stoich}$, s	2640	2676	1848	1876
total capacity, χ, g	17.1	18.9	43.3	45.3
time to max outlet temperature, $t(T_{g,max})$, s	1300	1497	510	650
max temperature rise, $\Delta T_{g,max}$, K	11.0	11.7	7.3	7.1
mean temperature rise, $\Delta T_{g,mean}$, K	3.6	4.8	1.8	2.0

* experimental data are not sufficiently resolved to determine the exact breakthrough time in test stand A

Table 6. Upper and lower bounds of model input parameters for uncertainty analysis.

parameter	test stand A		test stand B	
	lower bound	upper bound	lower bound	upper bound
linear-driving-force coefficient, k_n, s^{-1}	2.0×10^{-2}	2.2×10^{-2}	2.0×10^{-2}	2.2×10^{-2}
axial dispersion, D_{ax}, m^2/s	1.00×10^{-3}	1.20×10^{-3}	1.03×10^{-3}	1.22×10^{-3}
effective axial thermal conductivity, k_{eff}, W/(m K)	0.454	5.48	0.569	2.847
void fraction, ε	.343	.357	.343	.357
gas-adsorbent heat transfer coefficient, $h_{g\text{-}s}$, $W/(m^2K)$	91.4	238	105	276
gas-canister heat transfer coefficient, $h_{g\text{-}can}$, $W/(m^2K)$	12.9	25.9	8.3	16.5
canister-insulation heat transfer coefficient, $h_{can\text{-}ins}$, $W/(m^2K)$	0	∞	0	∞
insulation-ambient heat transfer coefficient, $h_{ins\text{-}amb}$, $W/(m^2K)$	2	25	2	25
adsorbent envelope density, ρ_{env}, kg/m^3	1168	1192	1167	1191

Table 7. Percent change in breakthrough time, stoichiometric breakthrough time, and total capacity from baseline case for model input parameters evaluated at their upper and lower uncertainty bounds as given in Table 6.

	breakthrough time				**stoichiometric breakthrough time**				**total capacity**			
	test stand A		**test stand B**		**test stand A**		**test stand B**		**test stand A**		**test stand B**	
parameter	**low**	**high**	**low**	**high**	**low**	**high**	**low**	**high**	**low**	**high**	**low**	**high**
k_n	-5.0%	4.0%	-6.3%	6.3%	-0.2%	0.1%	0%	0%	-0.3%	0.2%	-0.1%	0.1%
D_{ax}	24.0%	23.0%	0%	0%	0.5%	0.5%	0%	0%	0.7%	0.7%	0%	0%
k_{eff}	-1.0%	1.0%	0%	1.6%	0%	-0.1%	0%	0%	0%	-0.1%	0%	0%
ε	2.0%	-3.0%	3.2%	-3.2%	1.1%	-1.1%	1.1%	-1.1%	1.0%	-1.0%	1.1%	-1.1%
h_{g-s}	0%	0%	0%	0%	0%	0%	0%	0%	0%	0%	0%	0%
h_{g-can}	0%	-1.0%	0%	0%	0%	0%	0%	-0.1%	0%	0%	0.1%	-0.1%
$h_{can-ins}$	-1.0%	1.0%	0%	0%	-0.1%	0%	-0.1%	0.1%	-0.1%	0%	-0.1%	0.1%
$h_{ins-amb}$	0%	0%	0%	0%	0%	0.1%	0%	0.1%	-0.1%	0%	0%	0.1%
ρ_{env}	-2.0%	1.0%	-1.6%	3.2%	-1.0%	1.0%	-0.9%	1.1%	-1.0%	1.0%	-0.9%	1.1%

Table 8. Percent change in maximum/mean temperature rise across the bed from baseline model for model input parameters evaluated at their upper and lower uncertainty bounds as given in Table 6.

	time to max outlet temp.				max temperature rise				mean temperature rise			
	test stand A		test stand B		test stand A		test stand B		test stand A		test stand B	
parameter	**low**	**high**	**low**	**high**	**low**	**high**	**low**	**high**	**low**	**high**	**low**	**high**
k_n	-1.6%	1.6%	-6.3%	4.8%	-1.2%	1.2%	-0.5%	0.5%	-0.3%	0.3%	0%	0.2%
D_{ax}	7.0%	7.0%	0%	-1.6%	5.8%	5.8%	0%	0%	0.8%	0.8%	0.1%	0.1%
k_{eff}	-0.8%	3.1%	-1.6%	6.3%	0.3%	-3.9%	0.3%	-4.1%	0.2%	-2.5%	0.2%	-2.9%
ε	1.6%	-1.6%	1.6%	-3.2%	0.4%	-0.4%	0.1%	-0.1%	1.0%	-1.0%	1.1%	-1.0%
h_{g-s}	0%	0%	0%	0%	0%	0%	0%	0%	0%	0%	0.1%	0.1%
h_{g-can}	-1.6%	1.6%	-4.8%	6.3%	-0.8%	1.9%	1.9%	-3.2%	0%	0%	0.3%	0.2%
$h_{can-ins}$	0.8%	3.1%	0%	-1.6%	4.5%	-5.2%	0%	0.4%	4.7%	-3.8%	2.4%	0.3%
$h_{ins-amb}$	0%	-0.8%	0%	0%	0.2%	-1.4%	-0.1%	0.4%	0.8%	-2.9%	0.1%	0.4%
ρ_{env}	-1.6%	0.8%	-3.2%	1.6%	-0.3%	0.3%	0.3%	0.5%	-1.0%	0.9%	-0.5%	1.4%

For Table of Contents Only